Sarcomeric perturbations of myosin motors lead to dilated cardiomyopathy in genetically modified *MYL2* mice

Chen-Ching Yuan[a], Katarzyna Kazmierczak[a], Jingsheng Liang[a], Zhiqun Zhou[a], Sunil Yadav[a], Aldrin V. Gomes[b], Thomas C. Irving[c], and Danuta Szczesna-Cordary[a,1]

[a]Molecular and Cellular Pharmacology, University of Miami Miller School of Medicine, Miami, FL 33136; [b]Department of Neurobiology, Physiology, and Behavior, University of California, Davis, CA 95616; and [c]Department of Biological Sciences, Illinois Institute of Technology, Chicago, IL 60616

Edited by J. G. Seidman, Harvard Medical School, Boston, MA, and approved January 24, 2018 (received for review September 27, 2017)

Dilated cardiomyopathy (DCM) is a devastating heart disease that affects about 1 million people in the United States, but the underlying mechanisms remain poorly understood. In this study, we aimed to determine the biomechanical and structural causes of DCM in transgenic mice carrying a novel mutation in the *MYL2* gene, encoding the cardiac myosin regulatory light chain. Transgenic D94A (aspartic acid-to-alanine) mice were created and investigated by echocardiography and invasive hemodynamic and molecular structural and functional assessments. Consistent with the DCM phenotype, a significant reduction of the ejection fraction (EF) was observed in ∼5- and ∼12-mo-old male and female D94A lines compared with respective WT controls. Younger male D94A mice showed a more pronounced left ventricular (LV) chamber dilation compared with female counterparts, but both sexes of D94A lines developed DCM by 12 mo of age. The hypocontractile activity of D94A myosin motors resulted in the rightward shift of the force–pCa dependence and decreased actin-activated myosin ATPase activity. Consistent with a decreased Ca^{2+} sensitivity of contractile force, a small-angle X-ray diffraction study, performed in D94A fibers at submaximal Ca^{2+} concentrations, revealed repositioning of the D94A cross-bridge mass toward the thick-filament backbone supporting the hypocontractile state of D94A myosin motors. Our data suggest that structural perturbations at the level of sarcomeres result in aberrant cardiomyocyte cytoarchitecture and lead to LV chamber dilation and decreased EF, manifesting in systolic dysfunction of D94A hearts. The D94A-induced development of DCM in mice closely follows the clinical phenotype and suggests that *MYL2* may serve as a new therapeutic target for dilated cardiomyopathy.

MYL2 | myosin RLC | DCM | transgenic D94A mice | invasive hemodynamics

Dilated cardiomyopathy (DCM) is a heart disease characterized by left ventricular (LV) dilation, normal or reduced LV wall thickness, interstitial fibrosis, and significantly diminished contractile function (1). It is one of the most common cardiomyopathies, with a predicted occurrence of 1 in 400 in the United States (2). DCM may be sporadic and caused by ischemia, alcohol toxicity, or viral infection, or it can be genetic and arise from mutated genes. Inherited gene defects account for up to 25% of cases of DCM and include mutations in more than 40 different genes, including cytoskeletal, sarcomeric, sarcolemmal, and nuclear envelope proteins (3). In the family of sarcomeric proteins, mutations in at least nine genes encoding for myosin heavy chain (MHC), β-MHC (*MYH7*), α-MHC (*MYH6*), MyBP-C (myosin-binding protein C), titin, cardiac actin, troponin (Tn) complex, and α-Tm (tropomyosin) proteins are implicated in DCM (4). Recently, our group reported on a mutation in *MYL2*, encoding the myosin regulatory light chain (RLC), identified by exome sequencing in a pedigree with familial DCM (5). Biochemical studies of the recombinant aspartic acid-to-alanine RLC mutant (D94A-RLC) showed that subtle changes in the secondary structure of the RLC and its interaction with the MHC resulted in chemomechanical uncoupling and malfunction of D94A-mutated myosin motor protein (5).

Myosin RLC is a major regulatory subunit of striated-muscle myosin and a modulator of Ca^{2+} and tropomyosin–troponin–controlled regulation of cardiac muscle contraction (6). It is localized at the head–rod junction of the MHC and, together with the myosin essential light chain, stabilizes the α-helical neck region of the myosin head, also called the lever arm (7). To address the mechanisms responsible for triggering abnormal function of D94A-RLC myosin and cardiac defects consistent with DCM, we have generated transgenic (Tg) mice expressing the D94A-mutated human ventricular RLC. Age- and sex-matched Tg-WT (wild-type) mice, expressing human ventricular RLC and produced in this laboratory previously (8), served as controls. The Tg-D94A animal model is a clinically relevant rodent model of human familial DCM with a mutation in myosin RLC encoded by *MYL2* (5).

We provide strong evidence that the D94A mutation in cardiac myosin RLC controls contractility via structural alterations of myosin thick filaments and their interaction with the regulated actin filaments triggering an aberrant cross-bridge cycling and down-regulating myofilament response to Ca^{2+}. These changes ultimately result in significant reduction of the ejection fraction (EF) and progressive dilated cardiomyopathy in D94A-mutated

Significance

Dilated cardiomyopathy (DCM) is a progressive heart disease with no current cure, often culminating in heart transplantation. Transgenic D94A (aspartic acid-to-alanine) mice carrying a novel DCM-causative mutation in the *MYL2* gene, encoding the cardiac myosin regulatory light chain, were created and investigated by echocardiography and invasive hemodynamic and molecular structural and functional assessments. Our data show that hypocontractile myosin motors and structural perturbations at the level of sarcomeres trigger aberrant functional remodeling in D94A hearts and the development of DCM, which closely follows the clinical phenotype. Left ventricular chamber dilation and decreased ejection fraction, observed in D94A hearts, were indicative of systolic dysfunction, a hallmark of DCM. Our study suggests that *MYL2* may be considered a therapeutic target for dilated cardiomyopathy.

Author contributions: C.-C.Y. and D.S.-C. designed research; C.-C.Y., K.K., J.L., Z.Z., and S.Y. performed research; A.V.G. and T.C.I. contributed new reagents/analytic tools; C.-C.Y., K.K., J.L., Z.Z., S.Y., A.V.G., T.C.I., and D.S.-C. analyzed data; and D.S.-C. wrote the paper.

The authors declare no conflict of interest.

This article is a PNAS Direct Submission.

[1]To whom correspondence should be addressed. Email: dszczesna@med.miami.edu.

This article contains supporting information online at www.pnas.org/lookup/suppl/doi:10.1073/pnas.1716925115/-/DCSupplemental.

animals compared with respective WT-RLC control mice. Our in-depth study clearly shows that the *MYL2* variant, with the D94A mutation in the myosin RLC, closely follows the clinical DCM phenotype, providing a foundation for including the *MYL2* gene in the pool of ~40 currently screened DCM genes (3), and that the myosin ventricular RLC may be considered an additional therapeutic protein target for DCM.

Results

Generation of the D94A-RLC Animal Model of DCM. To address the mechanisms underlying cardiac dysfunction due to the D94A mutation in myosin ventricular RLC protein (UniProtKB P10916), we generated two lines (Ls) of the α-MHC–driven transgenic mice expressing the D94A-mutated human ventricular RLC (Fig. 1*A*). Female (F) and male (M) D94A-L1 and -L2 animals were used in the experiments, and the results were compared with age- and gender-matched Tg-WT-RLC mice (8). Direct assessment of the human (%) versus mouse (%) cardiac RLC in the ventricles of WT mice and in D94A-L1 and D94A-L2 by mass spectrometry showed the expression of 87.6 ± 4.8 versus 12.4 ± 4.9 (WT), 53.4 ± 3.2 versus 46.6 ± 3.2 (L1), and 49.5 ± 2.8 versus 50.5 ± 2.8 (L2) (Fig. 1*B*). Therefore, the generated model of DCM with ~50% of mutant RLC expression recapitulated the heterozygous transmission of the mutated allele in a D94A-positive family (5). No significant changes in RLC phosphorylation due to the D94A mutation occurred in the hearts of mice, as tested by 2D SDS/PAGE using mouse ventricular preparations (myosin and myofibrils) and RLC-specific antibodies (Fig. 1*C*). The latter result is consistent with our in vitro study showing that the phosphorylation of RLC by Ca^{2+}/calmodulin-activated myosin light chain kinase was not affected by D94A (5).

Ventricular Histology and Ultrastructure of D94A Hearts. Cardiac phenotypes in Tg-D94A lines were identical and showed biventricular cardiac dilation that was prominent by age ~5 mo in animals of both sexes, as evidenced by gross pathology images and those of longitudinal heart sections of D94A compared with WT mice (Fig. 2*A*). The myocardial ultrastructure assessed by transmission electron microscopy in ~9-mo-old D94A mice revealed myopathic vacuolar formations in the myocardium of

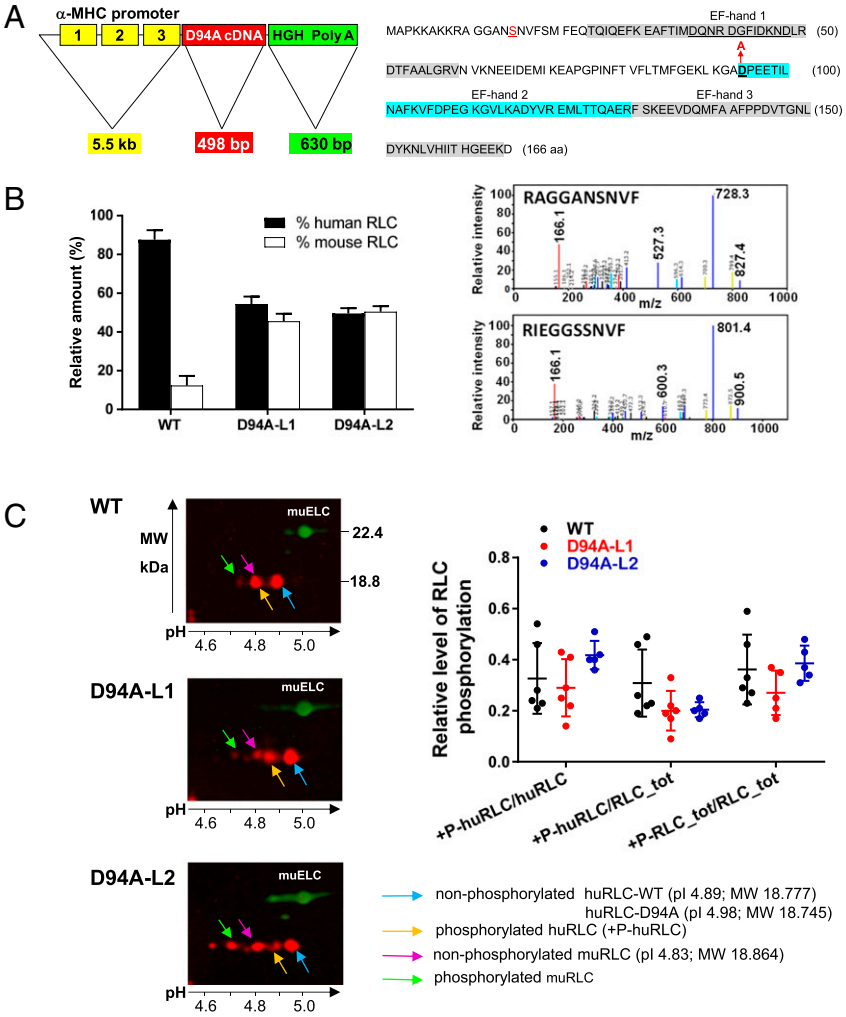

Fig. 1. (*A*) Transgene construct with α-MHC promoter for expression of the D94A-RLC mutant (*Left*) and amino acid sequence of human cardiac RLC UniProtKB P10916 (pI 4.89; molecular mass 18.789 kDa) (*Right*). HGH, human growth hormone. (*B*) Relative expression of D94A-RLC in Tg mice. (*B*, *Right*) Sample spectra of human (*Upper*) and mouse (*Lower*) RLC sequences. (*C*) Two-dimensional SDS/PAGE and Western blots of ventricular myosin from WT, D94A-L1, and D94A-L2 mouse lines. RLC proteins were visualized with the CT-1 antibody and the myosin essential light chain (ELC) protein (used as a loading control) with the monoclonal ab680 antibody (Abcam). Phosphorylated and nonphosphorylated human (huRLC-WT and huRLC-D94A) and mouse (muRLC) RLC proteins were separated according to their respective molecular masses and pI, and were quantitated using $n = 5$ or 6 myosin/myofibrillar preparations per line ±SD. No statistical difference in RLC phosphorylation was observed between WT, D94A-L1, and D94A-L2 mice, $P > 0.05$, using one-way ANOVA.

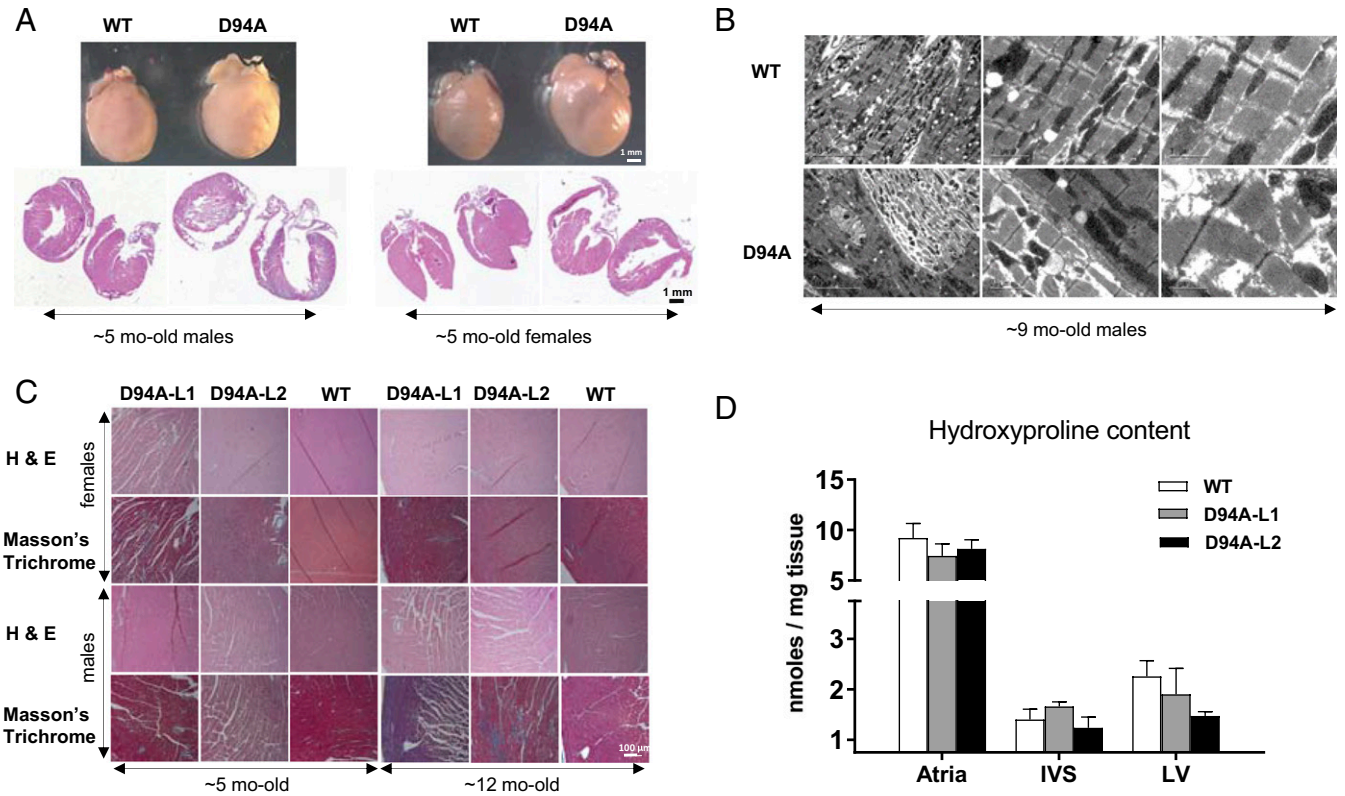

Fig. 2. (*A*) Hearts of representative ~5-mo-old male and female D94A mice and their longitudinal sections showing biventricular cardiac dilation compared with respective WT controls. (Scale bars, 1 mm.) (*B*) Transmission electron microscopy images of ~9-mo-old D94A-L1 vs. WT hearts. [Scale bars, 10 μm (*Left*), 2 μm (*Middle*), and 1 μm (*Right*).] Note excessive vacuolar formations in the myocardium of D94A vs. WT mice. (*C*) Hematoxylin and eosin- and Masson's trichrome-stained LV sections from ~5- and ~12-mo-old M and F D94A-L1 and -L2 vs. WT mice. (Scale bar, 100 μm.) (*D*) Hydroxyproline content in the hearts of 7- to 11-mo-old M and F D94A-L1 and -L2 compared with WT mice.

D94A versus WT mice and disrupted sarcomeric structures in the mutant compared with age- and sex-matched WT-RLC mice (Fig. 2*B*). Histopathology evaluation of left ventricular tissue from ~5- and ~12-mo-old D94A animals showed no obvious myofilament disarray or fibrosis, and the rare fibrotic depositions occurred in the hearts of older male but not female D94A mice (Fig. 2*C*). The lack of fibrosis in D94A mice was confirmed by a quantitative hydroxyproline (HOP) assay, which showed no difference in HOP content in atria, interventricular septum, or LV tissue between D94A lines and WT mice (Fig. 2*D*).

LV Chamber Dilation and Severely Reduced Ejection Fraction in D94A Hearts. As heart chamber size increased, D94A mice developed severely diminished cardiac function, as assessed by echocardiography and invasive hemodynamics (9, 10) (Fig. 3). Consistent with the DCM phenotype, a significant reduction of the ejection fraction and fractional shortening occurred in younger and older D94A-L1 and -L2 mice compared with respective WT controls (Table 1, Table S1, and Movies S1 and S2). A largely dilated left ventricular chamber (increased LVID) was observed in young male D94A mice compared with female counterparts, but both sexes of D94A lines developed progressive dilated cardiomyopathy by 12 mo of age (Fig. 3*A*, Fig. S1, and Table S1).

Systolic Dysfunction in Young and Old D94A Mice. Hemodynamic assessment and pressure–volume loop analysis of D94A versus WT hearts showed significantly decreased intact heart function in both age groups of D94A mice compared with respective WT mice (Fig. 3*B* and Movies S1 and S2). Older D94A mice demonstrated a more pronounced phenotype compared with younger D94A mice, and the diminished cardiac function was more severe in male than in female D94A mice (Fig. S1 and Table S1). Decreased stroke work, cardiac output, and prerecruitable stroke work in D94A versus WT animals were paralleled by significantly elevated end-systolic and end-diastolic volume) compared with respective WT mice (Fig. 3*B*, Table 1, and Table S1).

In addition, D94A animals showed elevated values of Ea (arterial elastance) compared with WT mice that were present in young and old D94A mice of both sexes (Fig. 3*B*). Increased Ea is a sympathetic response to compensate for reduced LV stroke volume, which is controlled by the autonomic nervous system (11) and may be responsible for the D94A-mediated reduction of mechanical efficiency and the ventricular–arterial decoupling (12).

Our combined data indicate that young and old D94A mice of both sexes clearly suffer from systolic dysfunction, and no diastolic disturbance (no changes in the relaxation constant; tau) was observed in 5- or 12-mo-old F and M D94A mice compared with respective WT controls (Fig. 3).

Abnormalities of Myofilament Contractility in Skinned and Intact Papillary Muscle Fibers from D94A Mice. Skinned papillary muscle strips isolated from 5-mo-old D94A mice demonstrated a decrease in the Ca^{2+} sensitivity of force, with ΔpCa_{50} ~0.13 and ~0.25 for D94A mice of both sexes compared with respective WT controls (Fig. 4*A* and Table 2). No significant changes between genotypes were observed in the ability of myosin to develop maximal contractile force and, except for D94A-L1-F, no changes in maximal tension at pCa 4 per cross-section of muscle were noted. A similar trend of decreased Ca^{2+} sensitivity of force with no changes in F_{max} was observed in older animals (Fig. 4*A* and Table 2). Both age groups of mice demonstrated a DCM characteristic rightward shift in the force–pCa dependence and a significantly reduced

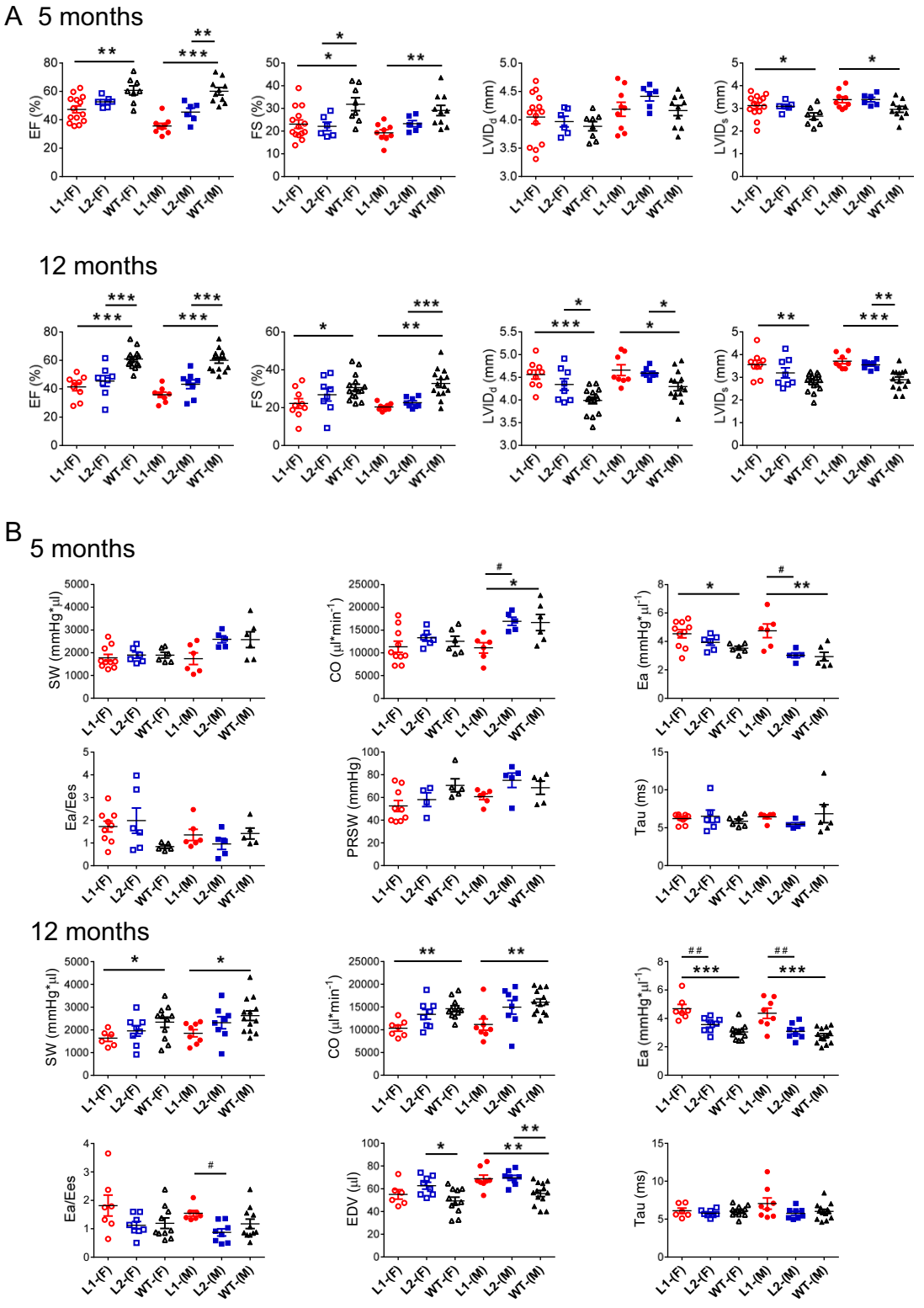

Fig. 3. In vivo characterization of heart morphology and function in D94A vs. WT lines by echocardiography (*A*) and invasive hemodynamics (*B*). Two lines of D94A (L1 and L2) female (open symbols) and male (closed symbols) were used and the results were compared with age- and sex-matched WT mice. CO, cardiac output; Ea, arterial elastance; EDV, end-diastolic volume; Ees, end-systolic elastance; EF, ejection fraction; FS, fractional shortening; LVID, left ventricular inner diameter in diastole (d) and systole (s); PRSW, prerecruitable SW; SW, stroke work; Tau, relaxation time constant. The number of F and M mice examined is given in Table 1. Data are the mean ± SEM. $^{*}P < 0.05$, $^{**}P < 0.01$, and $^{***}P < 0.001$ D94A vs. WT, $^{\#}P < 0.05$, and $^{\#\#}P < 0.01$ L1 vs. L2, by one-way ANOVA and the post hoc Tukey's multiple comparison test.

Table 1. Intact heart function in ~5-mo-old D94A-RLC mice compared with WT-RLC animals by echocardiography and invasive hemodynamics

Parameter	D94A-L1-F	D94A-L2-F	WT-F	D94A-L1-M	D94A-L2-M	WT-M
Echocardiography						
No. of animals	14	6	8	9	6	10
Heart/body, mg/g	4.63 ± 0.16	4.52 ± 0.36	4.48 ± 0.29	4.66 ± 0.12	5.15 ± 0.14	5.31 ± 0.21
Heart/tibia, mg/mm	7.01 ± 0.2	6.8 ± 0.19	6.69 ± 0.55	9.06 ± 0.27	10.34 ± 0.35*	8.74 ± 0.3[a]
HR, bpm	503 ± 9	498 ± 17	478 ± 17	512 ± 15	520 ± 11	497 ± 14
IVCT, ms	15.09 ± 1.01	12.48 ± 1.72	15.33 ± 1.6	15.49 ± 1.41	11.61 ± 1.11	15.09 ± 1.6
IVRT, ms	17.06 ± 1.5	14.92 ± 1.42	15.85 ± 0.9	15.76 ± 1.59	13.94 ± 0.46	14 ± 0.69
MV E/A	2.63 ± 0.24	1.83 ± 0.23	2.4 ± 0.29	1.88 ± 0.19	1.74 ± 0.17	1.91 ± 0.13
MV E/E′	−26.7 ± 2.4	−24.2 ± 2.8	−25.9 ± 2.0	−22.1 ± 1.3	−31.2 ± 2.1	−25.5 ± 2.4
EF, %	47 ± 2**	52 ± 1	60 ± 3	35 ± 2***,#,[a]	45 ± 2**,[a]	60 ± 2
FS, %	23 ± 1*	22 ± 2*	31 ± 3	19 ± 1[a],**	23 ± 1	29 ± 2
IVS;d, mm	0.81 ± 0.03	0.76 ± 0.03	0.74 ± 0.03	0.82 ± 0.06	0.87 ± 0.03	0.9 ± 0.04[a]
IVS;s, mm	1.09 ± 0.04	0.98 ± 0.06	1.09 ± 0.08	1.11 ± 0.09	1.13 ± 0.05	1.21 ± 0.08
LVID;d, mm	4.05 ± 0.11	3.97 ± 0.09	3.89 ± 0.08	4.19 ± 0.12	4.42 ± 0.08[a]	4.16 ± 0.1[a]
LVID;s, mm	3.12 ± 0.12*	3.09 ± 0.09	2.66 ± 0.14	3.38 ± 0.13*	3.39 ± 0.10*	2.96 ± 0.13
LVPW;d, mm	0.7 ± 0.03	0.71 ± 0.03	0.73 ± 0.02	0.8 ± 0.05	0.77 ± 0.04	0.78 ± 0.02
LVPW;s, mm	0.9 ± 0.05*	0.96 ± 0.05	1.06 ± 0.06	0.99 ± 0.06	1.06 ± 0.07	1.14 ± 0.04
Hemodynamics						
No. of animals	10	6	5	6	5	6
SW, mmHg×μL	1,779 ± 144	1,898 ± 137	1,896 ± 127	1,741 ± 259	2,592 ± 153[a]	2,577 ± 344
CO, μL/min	11,349 ± 1,155	13,330 ± 753	12,538 ± 1,109	11,106 ± 1,138*	16,938 ± 916[a]	16,673 ± 1,777
SV, μL	23.24 ± 2.06	24.99 ± 1.14	24.92 ± 1.11	21.78 ± 1.87*,#	31.54 ± 1.57[a]	32.86 ± 2.89[a]
ESV, μL	31.92 ± 3.46	30.65 ± 1.91	23.6 ± 2.26	45.95 ± 2.56*,[a]	41.22 ± 1.94[a]	34.31 ± 3.66[a]
EDV, μL	49.25 ± 4.09	50.39 ± 2.65	44.02 ± 1.8	62.49 ± 3.51	67.98 ± 2.35[a]	59.35 ± 4.49[a]
Pes, mmHg	100.2 ± 3.03*	97.31 ± 3.78	87.13 ± 3.21	99.6 ± 4.96	95.23 ± 1.59	92.23 ± 3.61
Ped, mmHg	5.48 ± 0.78	7.22 ± 2.29	5.42 ± 1.42	5.42 ± 1.09	4.91 ± 1.72	7.29 ± 1.8
HR, bpm	484 ± 16	532 ± 8	499 ± 25	506 ± 20	537 ± 12	504 ± 13
Ea, mmHg/μL	4.54 ± 0.28*	3.94 ± 0.21	3.53 ± 0.14	4.75 ± 0.48**	3.02 ± 0.17	2.93 ± 0.3
Ea/Ees	1.73 ± 0.22	1.99 ± 0.56	0.84 ± 0.08	1.36 ± 0.25	0.96 ± 0.25	1.42 ± 0.24
dP/dt_{max}, mmHg/s	9,339 ± 787	11,099 ± 1,794	9,249 ± 574	8,818 ± 659	9,010 ± 544	8,248 ± 575
dP/dt_{min}, mmHg/s	−9,428 ± 516	−9,593 ± 1,162	−9,133 ± 405	−8,496 ± 791	−9,655 ± 622	−8,784 ± 1,051
Tau, ms	6.22 ± 0.18	6.51 ± 0.82	5.87 ± 0.29	6.44 ± 0.23	5.46 ± 0.22	6.86 ± 1.18
No. of animals	9	4	5	6	5	5
ESPVR	3.24 ± 0.47	2.9 ± 0.76	4.24 ± 0.38	3.99 ± 0.81	4.39 ± 1.4	2.35 ± 0.52
EDPVR	0.15 ± 0.02	0.14 ± 0.02	0.16 ± 0.03	0.15 ± 0.06	0.10 ± 0.02	0.10 ± 0.01
PRSW	52.53 ± 4.59	58.09 ± 6.02	70.64 ± 5.78	60.69 ± 2.6	75.14 ± 6.35	68.64 ± 5.84
dP/dt_{max}-EDV	184.62 ± 21.3	184.78 ± 35.6	150.1 ± 19.66	172.61 ± 24.6	144.58 ± 15.8	117.44 ± 19.1

Heart weight/body weight (in mg/g); heart weight/tibia length (in mg/mm); CO, cardiac output; d, diastolic; dP/dt_{max}, peak rate for pressure rise; $-dP/dt_{min}$, peak rate for pressure decline; EDPVR, slope of end-diastolic PV relationship; EDV, end-diastolic volume; Ees, end-systolic elastance, slope of ESPVR (end-systolic pressure–volume relationship); ESV, end-systolic volume; FS, fractional shortening; HR, heart rate (in beats per min); IVCT, isovolumetric contraction time; IVRT, isovolumetric relaxation time; IVS, interventricular septum; LVID, left ventricular inner diameter; LVPW, LV posterior wall; MV E/A, mitral early (E)-to-late (A) diastolic inflow velocity; E′, early diastolic velocity; Ped, end-diastolic pressure; Pes, end-systolic pressure; PRSW, prerecruitable SW (slope of SW–EDV relationship); s, systolic; SV, stroke volume; SW, stroke work; Tau, relaxation time constant. Data are the mean ± SEM. *$P < 0.05$, **$P < 0.01$, and ***$P < 0.001$ D94A vs. WT, #$P < 0.05$ L1 vs. L2, by one-way ANOVA and the post hoc Tukey's multiple comparison test; [a]$P < 0.05$ M vs. F, by Student's t test.

contractile force at submaximal calcium concentrations (pCa 6 to 5). These data suggest that changes in the Ca^{2+}-dependent actin–myosin interactions trigger abnormal heart remodeling in D94A mice and result in decompensated cardiac systolic function (low EF) and dilated cardiomyopathy. Consistent with the D94A effects observed in this report, DCM-associated mutations in the thin-filament proteins studied in mice (deletion mutation ΔK210 in *TNNT2*) resulted in a diminished myofilament Ca^{2+} sensitivity with no changes in maximal contractile force (13).

We also investigated whether the changes in the force–pCa relationship observed in D94A mice originated from cellular calcium dysregulation or from abnormal myosin motor activity or other sarcomeric dysfunction. Force and calcium transients were measured in intact papillary muscle fibers from 6- to 8-mo-old D94A mice and age- and sex-matched WT mice using the IonOptix Calcium and Contractility Recording System (Fig. 4*B*). Electrically stimulated isometric twitches were recorded simultaneously with $[Ca^{2+}]$ transients after 1.5-h incubation with Fura-2 AM. No differences in peak force were found between the genotypes (Fig. 4*B*) but, consistent with the decreased myofilament Ca^{2+} sensitivity in skinned fibers, the relaxation phase of force transients was significantly faster (shorter time) in D94A compared with WT muscles (67 vs. 98 ms). No changes in intracellular $[Ca^{2+}]$ transients were observed (Fig. 4*B*). These data led us to the conclusion that the contractile properties of D94A-mutated myosin cross-bridges and their altered interaction with the thin filaments are most likely responsible for development of DCM in D94A animals.

Consistent with the lack of changes in myocellular calcium homeostasis, the gene expression profiles of the major intracellular players of the excitation–contraction coupling revealed no differences between D94A and WT hearts, and no differences were also noted between male and female mice (Fig. 4*C*). Total mRNA was isolated from the ventricles of three male and three female 5- to 6-mo-old D94A-L1 and from WT control mice. No D94A-mediated changes

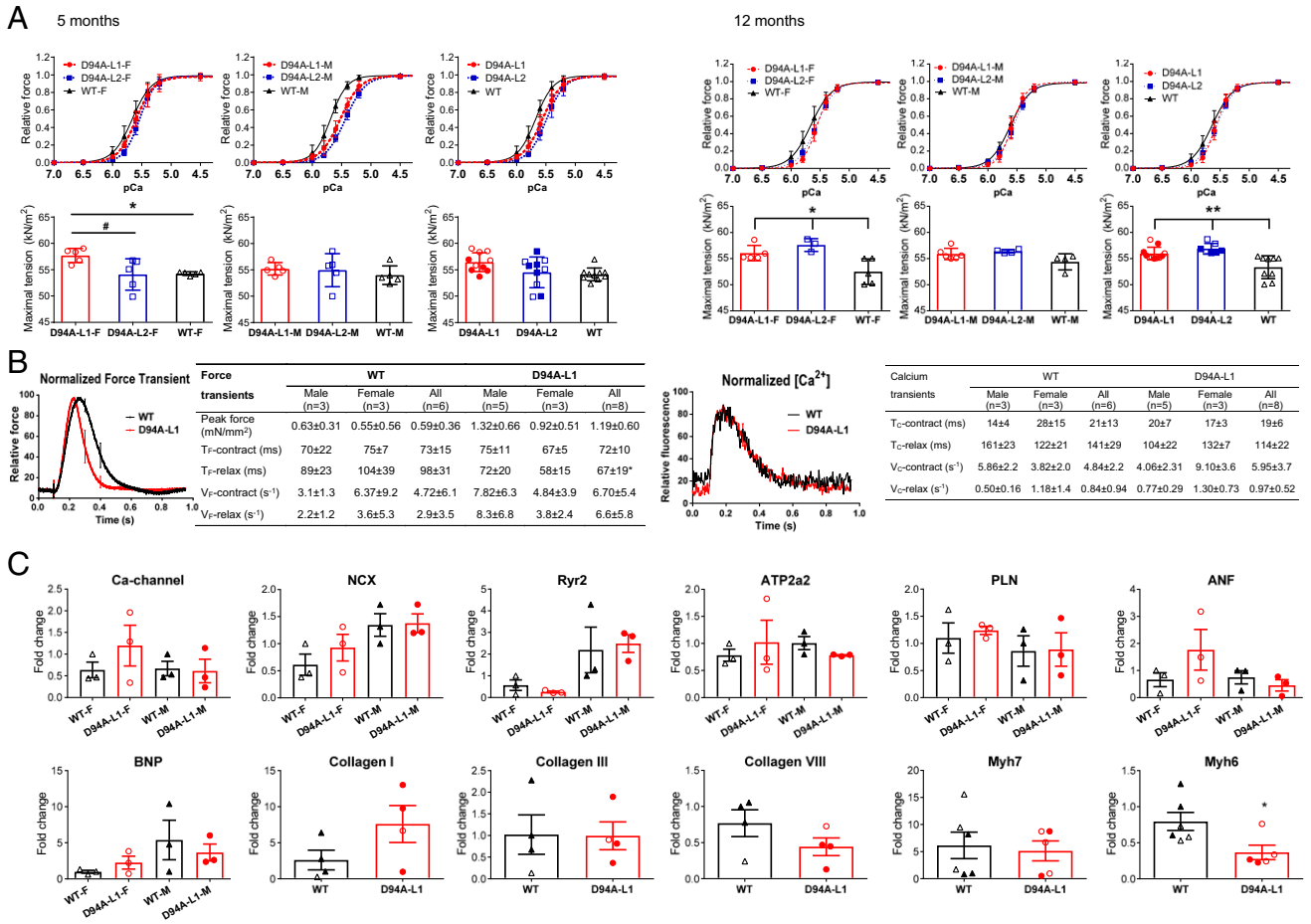

Force transients	WT			D94A-L1		
	Male (n=3)	Female (n=3)	All (n=6)	Male (n=5)	Female (n=3)	All (n=8)
Peak force (mN/mm²)	0.63±0.31	0.55±0.56	0.59±0.36	1.32±0.66	0.92±0.51	1.19±0.60
T_F-contract (ms)	70±22	75±7	73±15	75±11	67±5	72±10
T_F-relax (ms)	89±23	104±39	98±31	72±20	58±15	67±19*
V_F-contract (s^{-1})	3.1±1.3	6.37±9.2	4.72±6.1	7.82±6.3	4.84±3.9	6.70±5.4
V_F-relax (s^{-1})	2.2±1.2	3.6±5.3	2.9±3.5	8.3±6.8	3.8±2.4	6.6±5.8

Calcium transients	WT			D94A-L1		
	Male (n=3)	Female (n=3)	All (n=6)	Male (n=5)	Female (n=3)	All (n=8)
T_C-contract (ms)	14±4	28±15	21±13	20±7	17±3	19±6
T_C-relax (ms)	161±23	122±21	141±29	104±22	132±7	114±22
V_C-contract (s^{-1})	5.86±2.2	3.82±2.0	4.84±2.2	4.06±2.31	9.10±3.6	5.95±3.7
V_C-relax (s^{-1})	0.50±0.16	1.18±1.4	0.84±0.94	0.77±0.29	1.30±0.73	0.97±0.52

Fig. 4. (*A*) Contractile function in papillary muscle fibers from ∼5- and ∼12-mo-old D94A-L1 and -L2 vs. WT mice. Open symbols depict female and closed symbols indicate male animals. (*B*) The effect of D94A mutation on force and calcium transients in intact papillary muscles. The measurements were performed on intact papillary muscles from 6- to 8-mo-old gender-matched D94A-L1 (five M and three F) and WT (three M and three F) mice. Time (in milliseconds) to depart 50% (t_{50}) from t_0 to peak during contraction, and from peak to baseline during relaxation, is characterized by T_F-contract and T_F-relax (force transients) and T_C-contract and T_C-relax ([Ca^{2+}] transients). Maximum velocity of force departing from and returning to the baseline during muscle contraction and relaxation is reported as V_F-contract and V_F-relax (force transients) and V_C-contract and V_C-relax ([Ca^{2+}] transients). Note a significant (*$P < 0.05$) decrease in T_F-relax in D94A-L1 vs. WT fibers. Results are presented as the average ± SD of *n* animals with *$P < 0.05$ and **$P \leq 0.01$ for mutant vs. WT and $^{\#}P < 0.05$ for D94A-L1 vs. D94A-L2, using one-way ANOVA (*A*) or Student's *t* test (*B*). (*C*) Gene expression profiles in D94A and WT mice. Real-time qPCR was performed on three F (open symbols) and three M (close symbols) D94A-L1 and WT mice, and the results are presented as fold change in transcript expression in D94A vs. WT mice. Data are the mean ± SEM. *$P < 0.05$, using one-way ANOVA with the Tukey's multiple comparison test.

in the expression of voltage-dependent L-type calcium channel, alpha-1C (Ca^{2+} channel), sodium–calcium exchanger, cardiac ryanodine receptor (Ryr2), ATP2a2 (SERCA2), and phospholamban genes were observed compared with WT control hearts (Fig. 4*C*). No changes in *myh7* between genotypes were noted but, in agreement with reports on DCM patients (14), mRNA of *myh6* was significantly down-regulated in D94A animals (Fig. 4*C*). In addition, ANF and BNP, stress response genes, were slightly up-regulated in D94A-F compared with WT-F mice, but the difference between genotypes did not reach statistical significance (Fig. 4*C*).

Hypocontractility of D94A-RLC Myosin. To understand the effect of D94A on myosin motor function, actin-activated ATPase activity assays were conducted on cardiac myosin purified from ventricles of D94A and WT mice. Consistent with other DCM mutations in α-MHC motor proteins studied in mice (15), a significantly lower V_{max} was observed for D94A compared with WT myosin (Fig. 5*A*), suggesting a slower transition from the weakly (A·M·ATP ↔ A·M·ADP·Pi) to strongly (A·M·ADP ↔ A·M) bound D94A cross-bridges. No differences in the Michaelis–Menten constant (K_m) were noted between the groups. Significantly, this hypocontractile activity of D94A-mutated myosin motors reflects a diminished ability of myosin to hydrolyze ATP to produce energy for muscle contraction (Fig. 5*A*).

Fluorescence-based steady-state binding of D94A-myosin to pyrene-labeled F-actin under rigor (no ATP) conditions supports the ATPase data and shows a stronger interaction of myosin with actin for the mutant, suggesting slower myosin dissociation rates (Fig. 5*B*). Lower V_{max} of D94A-myosin could also be due to fewer myosin heads participating in the contractile cycle, and both scenarios indicate a mutation-induced hypocontractility of the myosin motor and a compromised chemomechanical cycle that contracts the sarcomere, leading to lower EF and systolic dysfunction in the D94A mouse model of DCM.

Small-Angle X-Ray Diffraction Patterns in D94A and WT Papillary Muscles. The interfilament lattice spacing ($d_{1,0}$) can be used to derive the center-to-center distance between two adjacent thick and thin filaments. The intensity ratio ($I_{1,1}/I_{1,0}$) is the ratio of the integrated intensity of the 1,1 equatorial reflection (representing density in the plane containing both thick and thin filaments) to that of the 1,0 equatorial reflection (reflecting density in the

Table 2. Contractile function in skinned papillary muscle fibers from ~5- and ~12-mo-old D94A-RLC mice compared with WT-RLC animals

Parameter	D94A-L1-F	D94A-L2-F	WT-F	D94A-L1-M	D94A-L2-M	WT-M	D94A-L1$_{ALL}$	D94A-L2$_{ALL}$	WT$_{ALL}$
Five-mo-old mice									
No. of animals (fibers)	5 (40)	5 (46)	5 (39)	5 (38)	5 (39)	5 (49)	10 (78)	10 (85)	10 (88)
F_{max}, kN/m^2	57.71 ± 1.36*,#	54.1 ± 2.98	54.27 ± 0.32	55.19 ± 1.18	54.94 ± 3.14	53.99 ± 1.76	56.45 ± 1.79	54.52 ± 2.92	54.13 ± 1.2
pCa$_{50}$	5.56 ± 0.08	5.54 ± 0.05*	5.67 ± 0.09	5.52 ± 0.06**,#	5.44 ± 0.01**	5.69 ± 0.07	5.54 ± 0.07**	5.49 ± 0.06**	5.68 ± 0.07
Hill coefficient	2.99 ± 0.68	3.61 ± 0.88	2.81 ± 0.29	2.8 ± 0.82	2.89 ± 0.61	3.25 ± 0.78	2.89 ± 0.72	3.25 ± 0.81	3.03 ± 0.6
Twelve-mo-old mice									
No. of animals (fibers)	5 (44)	3 (18)	5 (46)	5 (44)	4 (19)	4 (51)	11 (88)	7 (37)	9 (97)
F_{max}, kN/m^2	56.06 ± 1.47*	57.62 ± 1.22*	52.51 ± 2.45	55.89 ± 1.07	56.39 ± 0.35	54.38 ± 1.54	55.97 ± 1.2*	56.91 ± 0.99*	53.34 ± 2.21
pCa$_{50}$	5.55 ± 0.05	5.56 ± 0.01	5.66 ± 0.1	5.58 ± 0.06	5.56 ± 0.04	5.61 ± 0.05	5.57 ± 0.05*	5.56 ± 0.03*	5.64 ± 0.08
Hill coefficient	3.78 ± 0.35**,##	2.84 ± 0.25	2.65 ± 0.19	3.8 ± 0.29**,##	2.97 ± 0.45	2.71 ± 0.21	3.79 ± 0.3**,##	2.91 ± 0.36	2.68 ± 0.19

F_{max}, tension per cross-section of muscle; pCa$_{50}$, calcium concentration for half-maximal activation (Ca^{2+} sensitivity). Data are the mean ± SD of n (number of animals) experiments; *P < 0.05 and **P ≤ 0.01 for mutant vs. WT, and #P < 0.05 and ##P ≤ 0.01 for D94A-L1 vs. D94A-L2, using one-way ANOVA.

plane containing only thick filaments) (16). Both parameters ($d_{1,0}$ and $I_{1,1}/I_{1,0}$) are important metrics of sarcomeric structure that were previously shown to be sensitive to amino acid substitutions in any of the sarcomeric components (10, 17).

The equatorial X-ray patterns were collected simultaneously with the measurements of force at pCa 8 to 4 on skinned papillary muscles from D94A versus WT mice at sarcomere length 2.1 μm (10). While no changes due to the D94A mutation were found in $d_{1,0}$ (in nm), there was a significant decrease in $I_{1,1}/I_{1,0}$ ratio upon fiber activation (Fig. 6). The smaller $I_{1,1}/I_{1,0}$ in DCM versus WT mice indicates repositioning of the D94A-myosin cross-bridge mass closer to the thick-filament backbone (10, 17). We propose that this reduced $I_{1,1}/I_{1,0}$ ratio in D94A mice reflects less association of the myosin heads with the thin filaments and underlies the key structural change in the sarcomere that results in desensitization of myofilaments to Ca^{2+}. Consistent with this line of thinking, a significantly reduced Ca^{2+} sensitivity of force was measured in skinned papillary muscle fibers from D94A mutant versus WT mice (Fig. 4*A*). On the other hand, in accordance with no changes in maximal force developed by D94A muscle fibers (Fig. 4 *A* and *B*), no changes in the interfilament lattice spacing, $d_{1,0}$, was measured upon activation (at pCa 5.2) in D94A mice compared with WT (Fig. 6).

Discussion

Dilated cardiomyopathy is a severe pathology of the heart that can appear as a spectrum of symptoms, from subtle to severe, including congestive heart failure. Reduced contractile function and pathological remodeling of the heart are recognized clinical hallmarks of DCM, but the early molecular events that impair heart performance are unknown and require further investigation. Consistent with DCM characteristics in human patients carrying the D94A mutation in MYL2 (5), the D94A transgenic mouse model presents with ventricular chamber dilation, which is accompanied by a decreased ejection fraction and mild global left ventricular systolic dysfunction (Fig. 3). Although the histologic alterations include interstitial and replacement fibrosis, D94A animals do not demonstrate excessive fibrotic lesions and only mild fibrosis is observed in older D94A male hearts (Fig. 2). This result is consistent with findings of other studies on small or large animal models of DCM suggesting that myocyte hypertrophy and fibrosis are not prominent features in this form of cardiomyopathy despite changes in hemodynamics and LV chamber structure and function (15, 18).

In addition to occurrences of fibrosis in male and not female D94A hearts (Fig. 2), the diminished cardiac function was also observed to be more severe in male than in female D94A mice

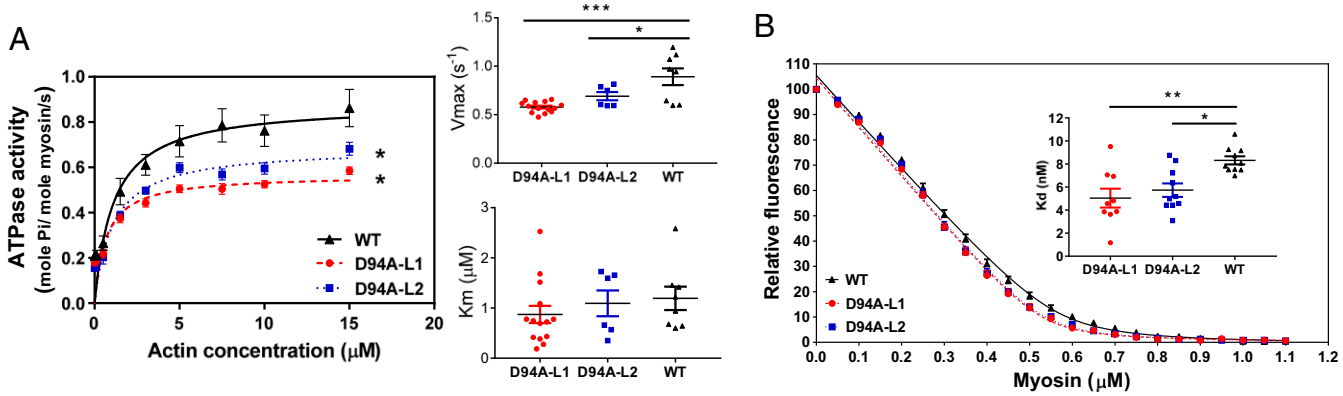

Fig. 5. (*A*) Actin-activated myosin ATPase activity of D94A and WT myosins. A significantly lower V_{max} was observed for D94A-L1 (0.57 ± 0.02 s^{-1}; n = 14) and D94A-L2 (0.69 ± 0.03 s^{-1}; n = 6) myosins compared with WT (0.88 ± 0.05 s^{-1}; n = 8). (*B*) Fluorescence-based binding assays of D94A or WT myosin to pyrene-labeled F-actin in the absence of ATP (rigor). Note a significantly higher binding affinity of D94A-L1 (K_d 4.48 ± 0.67 nM; n = 9) and D94A-L2 myosin (K_d 5.73 ± 0.58 nM; n = 10) vs. WT (K_d 8.31 ± 0.35 nM; n = 10) control. Both assays (*A* and *B*) were performed on myosin purified from left and right ventricles of 5- to 8-mo-old F and M D94A and WT mice. Approximately four or five hearts per group were used to generate one batch of myosin, and the assays were repeated with two to four different batches of myosin. No differences between the sexes were noted, and the data from M and F mice were pooled. Data are the mean ± SEM of n experiments with *P < 0.05, **P < 0.01, and ***P < 0.001 calculated, using one-way ANOVA with the Tukey's multiple comparison test.

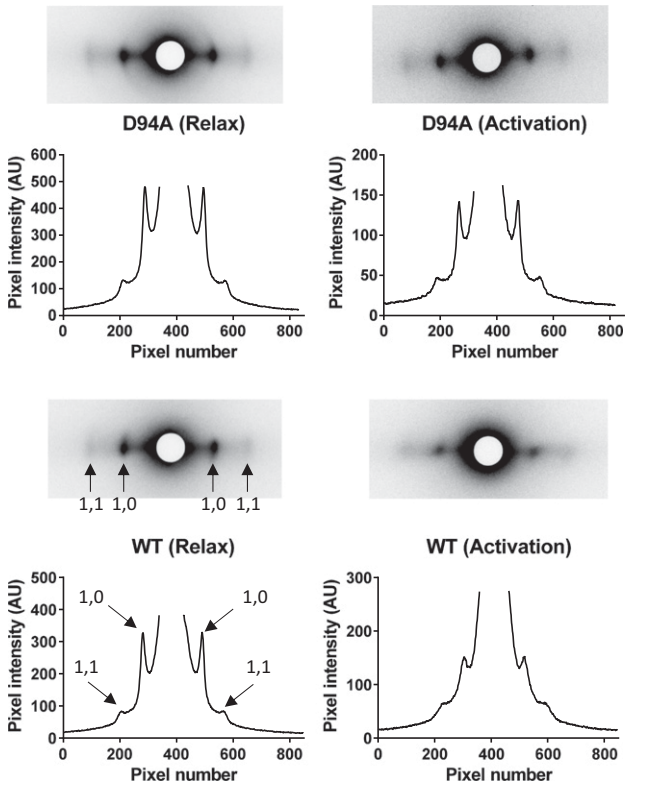

	WT	Nº fibers	D94A-L1	Nº fibers	P-value
Intensities ratio ($I_{1,1}/I_{1,0}$)					
pCa 8 (Relaxation)	0.22±0.06	15 (7F, 8M)	0.26±0.08	15 (8F, 7M)	0.206
pCa 5.2 (Activation)	0.43±0.02	14 (7F, 7M)	0.35±0.03*	12 (4F, 8M)	0.043
Lattice spacing ($d_{1,0}$ in nm)					
pCa 8 (Relaxation)	41.54±0.3	16 (8F, 8M)	41.38±0.24	15 (8F, 7M)	0.722
pCa 5.2 (Activation)	41.45±0.31	15 (7F, 8M)	41.64±0.29	14 (7F, 7M)	0.701

Fig. 6. Small-angle X-ray diffraction patterns and integrated intensity traces collected from papillary muscles from D94A-L1 (n = 3 F and 3 M mice) vs. WT (n = 4 F and 3 M mice) in relaxation (pCa 8) and activation (pCa 5.2). All patterns show clearly resolved 1,0 and 1,1 reflections. Note the significant difference in $I_{1,1}/I_{1,0}$ between D94A-L1 and WT (P = 0.043). Data are the mean ± SEM of n animals with *P < 0.05, using Student's t test.

(Fig. 3). A recent study has shown that in all cardiomyopathy subtypes there was an unequal sex distribution, with a tendency toward men for DCM, HCM (hypertrophic cardiomyopathy), and ARVC (arrhythmogenic right ventricular cardiomyopathy) and toward women for RCM (restrictive cardiomyopathy) (19). Reports also show that under disease conditions, females have higher expression of genes related to energy metabolism and can better maintain their metabolic function in response to a disease stimulus than males (20). Furthermore, significant sex differences in genes involved in the regulation of fibrosis and inflammation with a significant repression of these processes in women were also reported (21), indicating that females may be protected against effects of fibrosis and inflammation.

Previous studies have implicated different cytoskeletal and sarcomeric proteins in familial DCM, but the mechanisms by which these divergent mutations cause disease range from impairment of force transduction (22, 23) and disturbance of myocellular Ca^{2+} (24) to direct effects of sarcomeric protein mutations on myofilament Ca^{2+} sensitivity and contractile force generation, leading to systolic dysfunction and DCM (25). Creation of genetically altered transgenic and knockin mice expressing mutant proteins in their hearts provides valuable animal models to study the molecular mechanisms of DCM pathogenesis (13, 15, 26–29). Consistent with our results, mouse models of two MYH7 mutations (S532P and F764L) in an α-MHC background displayed depressed contractile function in isolated cardiomyocytes and a reduced ability of mutant myosins to translocate actin (V_{actin}) but had similar force-generating capacities (15). Thin-filament mouse models of DCM carrying disease-causing mutations in α-Tm (28) or troponin subunits (13, 29) demonstrated a largely reduced Ca^{2+} sensitivity and thus caused impairment of cardiac function through a malfunction of the Tm–Tn regulatory system. On the other hand, a knockin mouse model of DCM expressing a truncated form of MyBP-C (26) exhibited neonatal onset of a progressive DCM with myofibrillar disarray, fibrosis, and dystrophic calcification, but increased oxidative stress and myocardial inflammation were thought to underlie the diminished contractile response and heart failure in these mice (27, 30).

Small-angle X-ray diffraction patterns in skinned papillary muscles from D94A mice revealed distinct structural abnormalities in the sarcomeres of mouse hearts that may explain the underlying DCM phenotype. We demonstrate here that structural consequences of the D94A mutation in myosin RLC (Fig. 6) closely correlate with the functional abnormalities in D94A papillary muscle fibers (Table 2) and with abnormal heart function in echocardiography and invasive hemodynamics experiments (Table 1). The ability of D94A-mutated myosin to generate contractile force in skinned papillary muscle fibers at a level comparable to WT mice (Fig. 4*A*) correlated well with no changes in the interfilament lattice spacing ($d_{1,0}$) measured in D94A and WT fibers (Fig. 6). On the other hand, consistent with the reduced Ca^{2+} sensitivity of force observed in D94A fibers (Fig. 4*A*), a statistically significant decrease in $I_{1,1}/I_{1,0}$ ratio was measured in D94A fibers upon submaximal activation compared with WT (Fig. 6). A decrease in $I_{1,1}/I_{1,0}$ represents less association of the myosin heads with the thin filaments, which could explain the rightward shift in the force–pCa relationship in D94A versus WT fibers. Therefore, the structural changes in the D94A-RLC–mutated myosin motors stabilized their hypocontractile conformation (31) and led to desensitization of the myofilaments to calcium during force generation. These changes ultimately resulted in reduced ejection fraction and systolic abnormalities in D94A hearts.

The molecular pathogenesis of dilated cardiomyopathy was recently assessed in the context of the myosin superrelaxed state and interacting-heads motif (IHM) paradigm (31). Similar to the effects seen in this report (Fig. 5*A* and Table 2), DCM-causing mutations in MYH7 were shown to have modest effects on IHM interactions but have substantially reduced MHC motor functions, particularly nucleotide binding, resulting in reduced ATP consumption and decreased contractility. The authors elegantly demonstrated that genetic DCM and HCM variants differentially impact myosin motor functions and specific IHM interactions explaining the mechanisms for diminished contractile power in DCM and the distinctly compromised relaxation and energetics in HCM (31). Our data suggest that the D94A-RLC mouse model may be highly suitable for testing of novel myosin-specific therapeutics for systolic heart dysfunction, for example, omecamtiv mecarbil, aimed at increasing cardiac myosin activation and the duration of ejection without changing cardiomyocyte calcium homeostasis (32).

The results of this study strongly suggest that mice carrying the D94A-RLC mutation develop dilated cardiomyopathy by a mechanism involving direct effects of D94A on cardiac myosin, the molecular motor of the heart that transduces chemical energy from ATP hydrolysis into mechanical energy to drive cardiac

muscle contraction and support heart pump function to meet body demands for blood. Supporting this notion, the gene expression profiles of the major players in excitation–contraction coupling showed no differences between D94A and WT hearts (Fig. 4*C*). Studies on animal models of cardiomyopathy and human heart failure samples argue that dysregulation of RLC phosphorylation plays a role in the manifestation of the disease phenotype (10, 33, 34). However, in our previous in vitro study (5), as well as in this report, the D94A mutation did not reduce the overall RLC phosphorylation in the mutant myocardium compared with WT mice (Fig. 1*C*). Perhaps, as proposed by the Ferenczi group (35), the steady-state level of RLC phosphorylation in D94A mice may signify a compensatory adaptation to DCM pathology.

To conclude, D94A-mediated DCM is a rather complex issue, but clearly involves abnormal interactions between the hypocontractile myosin motors and actin–Tm–Tn filaments. The structural perturbations located at the level of sarcomeres result in aberrant cardiomyocyte cytoarchitecture leading to LV chamber dilation and decreased ejection fraction manifesting in systolic dysfunction of D94A hearts. Our comprehensive study demonstrates that this novel DCM MYL2 variant with the D94A mutation in the myosin RLC follows the clinical DCM phenotype, and suggests that in addition to other sarcomeric genes, MYL2 may serve as a therapeutic target for dilated cardiomyopathy disease.

Materials and Methods

Detailed materials and methods are outlined in *SI Materials and Methods*

This study conforms to the *Guide for the Care and Use of Laboratory Animals* published by the US National Institutes of Health (36). All protocols were approved by the Institutional Animal Care and Use Committee at the University of Miami Miller School of Medicine (assurance number A-3224-01, effective November 24, 2015). Euthanasia of mice was achieved through inhalation of CO_2 followed by cervical dislocation.

Generation of Transgenic DCM D94A-RLC Mice. The cDNA of human D94A-mutated ventricular RLC [National Center for Biotechnology Information (NCBI) accession no. NP_000423.2] was inserted downstream of the α-MHC promoter (clone 26, provided by Jeffrey Robbins, Cincinnati Children's Hospital Medical Center, Cincinnati, OH), and two Tg lines (D94A-L1 and D94A-L2) expressing mutated human RLC in mice were produced as described previously (8). The results were compared with previously produced Tg-WT mice expressing nonmutated human ventricular RLC (8). Relative expression of D94A mutant RLC in Tg lines was assessed by mass spectrometry (MS). SDS/PAGE bands of mouse purified myosin from four or five hearts per group were digested with trypsin and then reduced and alkylated. Digested peptides were analyzed by MS, and protein identification was determined using X! Tandem (9). Relative amounts of human versus mouse protein were determined by the ratio of the number of human-specific peptides (AGGANSN or EEVDQM) or mouse-specific peptides (IEGGSSN or EEIDQM) for which the most identified spectra were obtained (9, 37).

Heart Morphology and Function in D94A and WT Animals. Histopathology examination of paraffin-embedded longitudinal sections of whole mouse hearts stained with hematoxylin and eosin and Masson's trichrome, and the electron microscopy evaluation of myocardial ultrastructure, was assessed as described earlier (9, 10). Heart morphology and function were examined in male and female ∼5- and ∼12-mo-old D94A mouse lines (L1 and L2) and compared with age- and gender-matched WT mice by echocardiography and invasive hemodynamic assessments as outlined in detail in Yuan et al. (9, 10).

Myosin Cross-Bridge Contractile and Structural Properties in Skinned and Intact Fibers from D94A Versus WT Mice. Binding of D94A mouse purified myosin to pyrene–actin and actin-activated myosin ATPase activity assays were performed as previously reported (9, 10). Steady-state force development and force–pCa measurements were performed on skinned papillary muscle fibers with sarcomere length adjusted to 2.1 μm, according to previously described protocols (9). Approximately 5- and 12-mo-old D94A-L1 and -L2 animals were used with each heart, yielding on average 8 to 10 individual muscle strips. Force and $[Ca^{2+}]$ transient measurements were performed on intact papillary muscles from 6- to 8-mo-old sex-matched D94A-L1 (five M and three F) and WT (three M and three F) mice using the IonOptix Calcium and Contractility Recording System. Intact muscle fibers were stimulated at 1 Hz, and force and fluorescence (340/380 nm ratio) transients were recorded (8). The equatorial X-ray patterns were collected simultaneously with the measurements of force at pCa 8 to 4 on skinned papillary muscles from D94A-L1 (three F and three M) versus WT-RLC (four F and three M) mice at sarcomere length 2.1 μm (10).

Statistical Analysis. All values are shown as means ± SD or means ± SEM. Statistically significant differences between two groups were determined using an unpaired Student's *t* test, with significance defined as $*P < 0.05$, $**P < 0.01$, and $***P < 0.001$. Comparisons between multiple groups were performed using one-way ANOVA and the Tukey's multiple comparison test.

ACKNOWLEDGMENTS. This work was supported by NIH-HL123255 (to D.S.-C.), NIH-HL096819 (to A.V.G.), and NIH-NIGMS 9P41-GM103622 (to T.C.I.), and American Heart Association Grants 15PRE23020006 (to C.-C.Y.), 17PRE33650085 (to S.Y.), and 15POST25080302 (to Z.Z.). This research used resources of the Advanced Photon Source, a US Department of Energy (DOE) Office of Science User Facility operated for the DOE Office of Science by Argonne National Laboratory under Contract DE-AC02-06CH11357.

1. Halliday BP, Cleland JGF, Goldberger JJ, Prasad SK (2017) Personalizing risk stratification for sudden death in dilated cardiomyopathy: The past, present, and future. *Circulation* 136:215–231.
2. Hershberger RE, Hedges DJ, Morales A (2013) Dilated cardiomyopathy: The complexity of a diverse genetic architecture. *Nat Rev Cardiol* 10:531–547.
3. Pinto YM, et al. (2016) Proposal for a revised definition of dilated cardiomyopathy, hypokinetic non-dilated cardiomyopathy, and its implications for clinical practice: A position statement of the ESC working group on myocardial and pericardial diseases. *Eur Heart J* 37:1850–1858.
4. Piran S, Liu P, Morales A, Hershberger RE (2012) Where genome meets phenome: Rationale for integrating genetic and protein biomarkers in the diagnosis and management of dilated cardiomyopathy and heart failure. *J Am Coll Cardiol* 60:283–289.
5. Huang W, et al. (2015) Novel familial dilated cardiomyopathy mutation in MYL2 affects the structure and function of myosin regulatory light chain. *FEBS J* 282: 2379–2393.
6. Szczesna D (2003) Regulatory light chains of striated muscle myosin. Structure, function and malfunction. *Curr Drug Targets Cardiovasc Haematol Disord* 3:187–197.
7. Geeves MA (2002) Stretching the lever-arm theory. *Nature* 415:129–131.
8. Wang Y, et al. (2006) Prolonged Ca^{2+} and force transients in myosin RLC transgenic mouse fibers expressing malignant and benign FHC mutations. *J Mol Biol* 361: 286–299.
9. Yuan CC, et al. (2017) Hypercontractile mutant of ventricular myosin essential light chain leads to disruption of sarcomeric structure and function and results in restrictive cardiomyopathy in mice. *Cardiovasc Res* 113:1124–1136.
10. Yuan CC, et al. (2015) Constitutive phosphorylation of cardiac myosin regulatory light chain prevents development of hypertrophic cardiomyopathy in mice. *Proc Natl Acad Sci USA* 112:E4138–E4146.
11. Guarracino F, Baldassarri R, Pinsky MR (2013) Ventriculo-arterial decoupling in acutely altered hemodynamic states. *Crit Care* 17:213.
12. Borlaug BA, Kass DA (2008) Ventricular-vascular interaction in heart failure. *Heart Fail Clin* 4:23–36.
13. Du CK, et al. (2007) Knock-in mouse model of dilated cardiomyopathy caused by troponin mutation. *Circ Res* 101:185–194.
14. Carniel E, et al. (2005) Alpha-myosin heavy chain: A sarcomeric gene associated with dilated and hypertrophic phenotypes of cardiomyopathy. *Circulation* 112:54–59.
15. Schmitt JP, et al. (2006) Cardiac myosin missense mutations cause dilated cardiomyopathy in mouse models and depress molecular motor function. *Proc Natl Acad Sci USA* 103:14525–14530.
16. Millman BM (1998) The filament lattice of striated muscle. *Physiol Rev* 78:359–391.
17. Colson BA, et al. (2010) Differential roles of regulatory light chain and myosin binding protein-C phosphorylations in the modulation of cardiac force development. *J Physiol* 588:981–993.
18. Houser SR, et al.; American Heart Association Council on Basic Cardiovascular Sciences, Council on Clinical Cardiology, and Council on Functional Genomics and Translational Biology (2012) Animal models of heart failure: A scientific statement from the American Heart Association. *Circ Res* 111:131–150.
19. Elliott P, et al.; EORP Cardiomyopathy Registry Pilot Investigators (2016) European cardiomyopathy pilot registry: EURObservational Research Programme of the European Society of Cardiology. *Eur Heart J* 37:164–173.
20. Regitz-Zagrosek V, Kararigas G (2017) Mechanistic pathways of sex differences in cardiovascular disease. *Physiol Rev* 97:1–37.
21. Kararigas G, et al. (2014) Sex-dependent regulation of fibrosis and inflammation in human left ventricular remodelling under pressure overload. *Eur J Heart Fail* 16: 1160–1167.
22. Perriard JC, Hirschy A, Ehler E (2003) Dilated cardiomyopathy: A disease of the intercalated disc? *Trends Cardiovasc Med* 13:30–38.
23. Arber S, et al. (1997) MLP-deficient mice exhibit a disruption of cardiac cytoarchitectural organization, dilated cardiomyopathy, and heart failure. *Cell* 88:393–403.

24. Schmitt JP, et al. (2003) Dilated cardiomyopathy and heart failure caused by a mutation in phospholamban. *Science* 299:1410–1413.
25. Nonaka M, Morimoto S (2014) Experimental models of inherited cardiomyopathy and its therapeutics. *World J Cardiol* 6:1245–1251.
26. McConnell BK, et al. (1999) Dilated cardiomyopathy in homozygous myosin-binding protein-C mutant mice. *J Clin Invest* 104:1235–1244, and erratum (1999) 104:1771.
27. Lynch J, et al. (2005) Calreticulin signals upstream of calcineurin and MEF2C in a critical Ca(2+)-dependent signaling cascade. *J Cell Biol* 170:37–47.
28. Rajan S, et al. (2007) Dilated cardiomyopathy mutant tropomyosin mice develop cardiac dysfunction with significantly decreased fractional shortening and myofilament calcium sensitivity. *Circ Res* 101:205–214.
29. Davis J, et al. (2016) A tension-based model distinguishes hypertrophic versus dilated cardiomyopathy. *Cell* 165:1147–1159.
30. Lynch TL, IV, et al. (2017) Cardiac inflammation in genetic dilated cardiomyopathy caused by MYBPC3 mutation. *J Mol Cell Cardiol* 102:83–93.
31. Alamo L, et al. (2017) Effects of myosin variants on interacting-heads motif explain distinct hypertrophic and dilated cardiomyopathy phenotypes. *eLife* 6:e24634.
32. Malik FI, et al. (2011) Cardiac myosin activation: A potential therapeutic approach for systolic heart failure. *Science* 331:1439–1443.
33. Sheikh F, et al. (2012) Mouse and computational models link Mlc2v dephosphorylation to altered myosin kinetics in early cardiac disease. *J Clin Invest* 122:1209–1221.
34. van der Velden J, et al. (2003) The effect of myosin light chain 2 dephosphorylation on Ca^{2+}-sensitivity of force is enhanced in failing human hearts. *Cardiovasc Res* 57: 505–514.
35. Toepfer C, et al. (2013) Myosin regulatory light chain (RLC) phosphorylation change as a modulator of cardiac muscle contraction in disease. *J Biol Chem* 288:13446–13454.
36. National Research Council (2011) *Guide for the Care and Use of Laboratory Animals* (Natl Acad Press, Washington, DC), 8th Ed.
37. Liu H, Sadygov RG, Yates JR, III (2004) A model for random sampling and estimation of relative protein abundance in shotgun proteomics. *Anal Chem* 76:4193–4201.

Supporting Information

Yuan et al. 10.1073/pnas.1716925115

Study Design

The main aim of this study was to determine the mechanisms underlying cardiac dysfunction in mice carrying a novel mutation in the *MYL2* gene, encoding the myosin RLC, and identified by exome sequencing of three adult first-degree relatives who met the formal criteria for idiopathic DCM. Experimental studies (1–4) were performed using two transgenic (Tg) mouse lines expressing the D94A mutation of the human ventricular RLC (UniProtKB P10916), and the results were compared with those for Tg-WT mice. (*i*) Analysis of Tg human ventricular RLC expression (D94A and WT) directly in D94A ventricles was assessed by mass spectrometry and RLC phosphorylation status by 2D SDS/PAGE. (*ii*) Characterization of heart morphology and function was achieved by echocardiography and invasive hemodynamics. (*iii*) Determination of contractile function of D94A-RLC–containing myosin was assessed in papillary muscle fibers and in vitro by ATPase activity assays and actin–myosin binding. (*iv*) The mechanism of action for the D94A mutation was further studied by X-ray diffraction of papillary muscle fibers from mice. Two age groups (~5 and ~12 mo old) of both sexes (male, M; female, F) of mice were used to evaluate heart function in two lines of Tg-D94A-L1 and Tg-D94A-L2 mice and compared with Tg-WT controls. The sample size for the in vivo studies varied (n = 4 to 14 animals per group) because of unknown effects size and mortality during invasive hemodynamics study. The sample size for the in vitro experiments (n = 2 to 4 batches of myosin obtained from four or five hearts per group) was based on power analysis to detect an effect based on investigator's experience. Outlier data were not excluded. Exact numbers for each experiment are included below and in the respective tables and/or figure legends. The investigators were genotype-blinded when conducting echo/hemodynamics experiments, and the animals were randomly assigned for evaluation in two groups of D94A-L1 and D94A-L2 versus WT mice.

SI Materials and Methods

Tandem Mass Spectrometry Analysis and 2D SDS/PAGE. Proteins were run on SDS/polyacrylamide gels and stained with a mass spectroscopy-compatible Coomassie blue stain (1). Bands of interest were excised and destained with 40% methanol (vol/vol). In-gel trypsin digestion of myosin bands was carried out as previously described (1). Briefly, proteins in the gel were reduced with the reducing agent Tris(2-carboxyethyl)phosphine (10 mM) and alkylated with 100 mM 2-iodoacetamide. Trypsin (Promega Gold sequencing grade) was used, and digestion was allowed to proceed overnight at 37 °C. The resulting peptides were extracted from gel plugs with ammonium bicarbonate containing 1% (vol/vol) trifluoroacetic acid.

LC–MS/MS. Digested peptides were analyzed by LC–MS/MS using a Q Exactive Plus Orbitrap mass spectrometer (Thermo Scientific) with an attached Proxeon nanospray source and a Waters UPLC as previously described (2, 3).

Protein Identification and Data Analysis. Protein identification and quantification were performed with X! Tandem using both human and mouse databases. Parameters used included cleavage semi set as yes, missed cleavage sites set at 2; static modifications: carbamidomethyl (C); variable modifications: oxidation (M), deamidation (N, Q). The fragment mass tolerance was set at 0.1 Da and the precursor mass tolerance was set at 20 ppm. Peptide spectra (spectral count) unique to human and mouse myosin heavy chain identified by X! Tandem in each SDS/PAGE band were then tabulated and used to determine the relative abundance of the human and mouse MHC. The N-terminal peptides AGGANSN (human) and IEGGSSN (mouse) were used as unique peptides for quantification except when the number of these peptides detected was less than 50; instead, EEVDQMF (human) and (EEIDQMF) for mouse were used. Spectral count has been shown to be a reliable index for relative protein quantification, showing a dynamic range of two orders of magnitude (2, 3).

Assessment of Fibrosis by Hydroxyproline Assay. To assess the extent of fibrosis and collagen content in the hearts of mice, ~20 mg of flash-frozen tissue from interventricular septum (IVS) or left ventricles, ~6 mg from atria were processed as described in Yuan et al. (3). The samples were isolated from 7- to 11-mo-old female and male D94A-L1 (n = 4), D94A-L2 (n = 2), and WT (n = 4) mice and boiled in 200 μL of 6 M HCl at 110 °C overnight. Five-microliter aliquots of hydrolyzed tissue were added to 80 μL of 100% isopropanol, and allowed to react with 40 μL of 7% chloramine-T solution mixed at a 1:4 ratio with acetate citrate buffer [0.695 M sodium acetate, 0.174 M citric acid, 0.435 M NaOH, and 38.5% (vol/vol) isopropanol] for 5 min at room temperature. Then, 0.5 mL Ehrlich reagent (Ehrlich stock solution: 6 g of *p*-dimethylaminobenzaldehyde mixed with 20 mL of ethanol and 1.35 mL of sulfuric acid) was added to the mixture at a 3:13 ratio with isopropanol and incubated at 55 °C for 30 min. Then the mixture was placed on ice for 5 min and centrifuged at 5,000 × g for 1 min at 4 °C. Two-hundred-microliter aliquots were placed in a 96-well plate and the absorbance was measured at 558 nm. The standard curve of *trans*-4-hydroxy-L-proline (0 to 1,000 μM) was used to determine the total amount of hydroxyproline in atria, IVS, and LV (mg) of all tested mice.

Echocardiography and Invasive Hemodynamic Assessments. In vivo cardiac morphology and function studies on ~5- and ~12-mo-old mice were performed with a Vevo 2100 Imaging System (VisualSonics) equipped with an MS400 transducer. The mice were anesthetized by inhalation of 1 to 2% isoflurane and body temperature was maintained at 37 °C. The M-mode and B-mode images were saved for analysis of cardiac morphology and function using Vevo Lab 1.7.1 software (VisualSonics). Determined parameters included LV end-diastolic and end-systolic dimensions, LV posterior and anterior wall thickness, and ejection fraction. End-diastolic and end-systolic endocardial volumes were calculated from the bidimensional long-axis parasternal views 1, 5. Left ventricular diastolic function was analyzed using the values derived from mitral flow inflow velocity curves obtained by pulsed Doppler mode (3).

For invasive hemodynamic evaluation, mice were anesthetized by intubation with 1 to 2% isoflurane and body temperature was maintained at 37 °C. A 6% albumin solution was infused into the jugular vein at the rate of 5 μL/min. A catheter (SPR-839; Millar Instruments) transducer was introduced into the left ventricle through the right carotid artery. The pressure–volume (P–V) loops were recorded at steady state and during the inferior vena cava occlusion. The volume was calibrated by echocardiographic measurement of the end-diastolic volume and stroke volume. Diastolic performance was assessed by the measurement of the peak rate of left ventricular relaxation ($-dP/dt_{min}$), end-diastolic P–V relationship, and time constant of ventricular relaxation tau (in ms). The contractility was determined by the slope of the

end-systolic P–V relationship, and other parameters of systolic function included the preload recruitable power stroke work and peak rate of rise in the LV pressure–end-diastolic volume relationship (dP/dt_{max}–EDV) (3–5).

Myosin Motor Function and RLC Phosphorylation in D94A Versus WT Mice. Binding of D94A mouse purified myosin to pyrene–actin and actin-activated myosin ATPase activity assays were performed as previously reported (3). Briefly, myosin was extracted from the left and right ventricles of 4- to 8-mo-old F and M mice. Approximately five hearts per group were used to generate one batch of myosin, and the experiments were repeated with two to four different batches of myosin. For fluorescence-based binding studies, rabbit skeletal F-actin was labeled with pyrene iodoacetamide (Invitrogen/Molecular Probes). Pyrene-labeled F-actin (at 0.5 μM), stabilized by 0.5 μM phalloidin, was titrated with increasing concentrations of mouse purified cardiac myosin. Experiments were performed in a 2-mL cuvette in a buffer containing 0.4 M KCl and 10 mM Mops (pH 7.0). Quenching of pyrene fluorescence of F-actin on myosin binding was monitored using a Jasco 6500 fluorometer, with excitation at 340 nm and emission at 407 to 409 nm. Data points were fitted with a nonlinear binding equation yielding an apparent dissociation constant (K_d) (6). Actin-activated myosin ATPase activity was measured as a function of actin concentration in a 96-well microplate. The assay was performed in duplicate in a final volume of 120 μL in a buffer consisting of 25 mM imidazole (pH 7.0), 4 mM $MgCl_2$, 1 mM EGTA, and 1 mM DTT. The final KCl concentration was 78 mM. The reactions (run in duplicate) were initiated with the addition of 2.5 mM ATP with mixing in a Jitterbug incubator shaker (Boekel), allowed to proceed for 15 min at 30 °C, and then terminated by the addition of 5% trichloroacetic acid. The inorganic phosphate was determined as described previously (3). Data were analyzed using the Michaelis–Menten equation yielding V_{max} and K_m (3, 5).

RLC phosphorylation was assessed in mouse myosin purified from the left and right ventricles of 5- to 8-mo-old D94A-L1 and D94A-L2 mice and compared with age-matched WT using 2D SDS/PAGE. The proteins were separated based on charge differences, with human ventricular RLC-WT pI ∼4.89 and mouse ventricular RLC pI ∼4.83. RLC phosphorylation was detected in each preparation of mouse purified myosin with a phospho-specific RLC antibody that recognizes the phosphorylated form of the RLC and does not react with nonphosphorylated RLC (5), followed by a secondary goat anti-rabbit antibody conjugated with IR red 800 (Rockland). In blots of phosphorylated RLCs, the total RLC protein was detected with the CT-1 antibody, which served as a loading control (5). Respective dots were quantified with ImageJ software (https://imagej.nih.gov/ij/) and the following ratios were determined: +P-huRLC/huRLC, +P-huRLC/$RLC_{tot(ms+hu)}$, and +P-RLC_{tot}/RLC_{tot}.

Gene Expression Profiles by Real-Time qPCR. Total RNA (1.5 μg) from each heart of ∼5-mo-old male and female D94A-L1 versus WT mice was converted to double-stranded cDNA using Random Primers and a High-Capacity cDNA Reverse Transcription Kit (Applied Biosystems), and reverse transcription was performed as described before (3). Quantitative PCR was conducted using SYBR Green I chemistry with gene-specific QuantiTect Primer Sets (Qiagen) for murine Cacna1C (Ca-channel subunit a1, cardiac; NCBI accession no. NM_001159533); Slc8a1 (solute carrier family 8, sodium/calcium exchanger, NCX, member 1; NM_001112798); Ryr2 (ryanodine receptor 2, cardiac; NM_023868); ATP2a2 (SERCA2; NM_001110140); PLN (phospholamban; NM_001141927); ANF (atrial natriuretic factor; NM_008725); BNP (B-type natriuretic peptide; NM_008726); Col1a1 (collagen type I alpha I; NM_007742); Col3a1 (collagen type III alpha I; NM_009930); Col8a1 (collagen type VIII, alpha I; NM_007739); Myh7 (β-myosin heavy chain, cardiac; NM_080728); and Myh6 (α-myosin heavy chain, cardiac; NM_010856). GAPDH (glyceraldehyde-3-phosphate dehydrogenase; NM_008084) was used as a housekeeping gene. Primer sets and Power SYBR Green PCR Master Mix (Applied Biosystems) were used according to the manufacturer's protocol (3).

Steady-State Force Development and Force–pCa Relationship. Papillary muscles were isolated from left ventricles of ∼5- or ∼12-mo-old D94A-L1, D94A-L2, and WT mice and dissected to muscle bundles (∼2 × 0.5 mm) in ice-cold pCa 8 solution that contained 30 mM 2,3-butanedione monoxime (BDM) and 15% glycerol (5). The composition of pCa 8 solution was 10^{-8} M Ca^{2+}, 1 mM Mg^{2+}, 7 mM EGTA, 2.5 mM $MgATP^{2-}$, 15 mM creatine phosphate, and 20 mM Mops, ionic strength adjusted to 150 mM with K^+-propionate and pH adjusted to 7.00. After dissection, the bundles were transferred to pCa 8 solution mixed with 50% glycerol (storage solution) and incubated for 1 h on ice. Then the strips were transferred to fresh storage solution mixed with 1% Triton X-100 for 24 h at 4 °C. The bundles were finally transferred to a fresh storage solution and kept at −20 °C for 2 to 5 d (3, 5). On the day of the experiment, muscle bundles were dissected into small strips (∼1.5 mm in length and ∼100 μm in diameter), rinsed three times in pCa 8 solution, and attached to a Guth force transducer (3). They were then soaked in pCa 8.0 solution containing 15 units per mL of creatine phosphokinase (to complete the ATP regeneration system; present in all pCa solutions) for a few minutes followed by further skinning for 30 min in pCa 8 solution that contained 1% Triton X-100. After rinsing three times in pCa 8 solution, their length was adjusted to remove the slack. This procedure resulted in a sarcomere length of ∼2.1 μm as judged by first-order optical diffraction using an HeNe laser (wavelength 0.6328 μm) (3). The strips were then relaxed in pCa 8 solution and the maximal force was determined in pCa 4 solution (same composition as pCa 8 except $[Ca^{2+}]$ 10^{-4} M). After maximal force determination, the strips were exposed to solutions of increasing concentration of Ca^{2+} (pCa 8 to 4) and the force–$[Ca^{2+}]$ relationship was established. The data were plotted and analyzed using the Hill equation yielding the pCa_{50} value (Ca^{2+} concentration that produces half-maximal activation) and the Hill coefficient (n_H) (3, 5).

Intact Fiber Experiments. Following euthanasia, the hearts were rapidly excised and rinsed in Krebs–Ringer solution supplemented with 30 mM BDM. Intact papillary muscles were carefully dissected from the left ventricle in preoxygenated (95% O_2/5% CO_2) BDM–Krebs–Ringer solution to minimize cutting injury. Krebs–Ringer solution contained 152 mM Na^+, 3.6 mM K^+, 135 mM Cl^-, 25 mM HCO_3^-, 0.6 mM Mg^{2+}, 1.3 mM $H_2PO_4^-$, 0.6 mM SO_4^{2-}, 2.5 mM Ca^{2+}, and 5.6 mM glucose (7). Muscle preparations were incubated in BDM–Krebs–Ringer buffer containing 50 μM Fura-2 AM (Life Technologies) dissolved in DMSO and 0.1% pluronic acid at room temperature for 1.5 h in the dark, followed by three washes in BDM–Krebs–Ringer solution to remove excess Fura-2 AM. Muscle fibers were then mounted in a flow chamber between a hook connected to a length-controlled micromanipulator and a force transducer (custom-made by Brad Palmer, IonOptix, LLC, University of Vermont, Burlington, Vermont) via platinum foil clips. Preoxygenated Krebs–Ringer solution (95% O_2, 5% CO_2; pH 7.4) was perfused into the chamber at a flow rate of about 2 mL/min. The temperature in the muscle chamber was kept constant at 25 °C by a heat exchanger at the inflow line and a circulating water bath. The muscle was stretched to an optimum length at which the developed tension was maximal during an isometric twitch. Sarcomere length was monitored by a camera and maintained at 2.1 to 2.2 μm for another 10 to 15 min to allow the force development to stabilize. Stimulus was applied through platinum

hooks and strength was adjusted to 20% above threshold (about 5 to 7 V) at a frequency of 1 Hz for papillary muscles. The cross-sectional area of each muscle was used to normalize the developed force, which allowed for comparison between muscles of different diameters. Contractile force was recorded, and force data are presented in mN/mm^2. The unique hyperSwitch dual-excitation light source with submillisecond switching times, an inverted fluorescence microscope equipped with a calcium photometry objective, and MyoCam-S digital variable field rate CCD video system were used to detect and record the calcium ion transient of the intact fibers loaded with Fura-2 AM, a dual-excitation indicator dye (IonOptix, LLC) (8). Fura-2 AM fluorescence was collected by a CCD camera from 340- and 380-nm channels, followed by background subtraction. The dynamic measurement allowed up to 1,000 length recordings per s. Each set of data was averaged from ∼20 force–calcium transient peaks and analyzed using the system's IonWizard software. Student's *t* test was used to analyze statistical significance between D94A and WT by male/female/both sexes separately, and one-way ANOVA was used to compare between groups. Force and $[Ca^{2+}]$ measurements were performed on 6- to 7.5-mo-old D94A mice (five M and three F) versus 5.5- to 7.5-mo-old WT mice (three M and three F).

Small-Angle X-Diffraction Study. Equatorial X-ray diffraction patterns were collected from freshly skinned papillary muscle strips from D94A-L1 and WT mice, mounted in an X-ray chamber, using the small-angle instrument at BioCAT beamline 18ID at the Advanced Photon Source, Argonne National Laboratory, as described previously (3). X-ray exposures were 1 s at an incident flux of $\sim 1 \times 10^{12}$ photons per s. X-ray focal spots were about 0.5 × 0.5 mm at the sample and 0.06 × 0.15 mm at the detector. Sample-to-detector distance was 3 m and X-ray wavelength was 0.103 nm. Sarcomere length was adjusted to 2.1 μm by laser diffraction using a 4-mW HeNe laser (3). Simultaneous force and diffraction pattern measurements were performed in each of six pCa solutions (pCa 8 to 4). Solutions were changed using a syringe pump equipped with multiway valves (Hamilton model 500). Isolated fibers were mounted between a force transducer (Aurora Scientific model 402A) and a servo motor (Aurora Scientific model 308B). Force and length were monitored by digital controller (Aurora Scientific Model 600A). Diffraction patterns were collected only at the plateau phase of force developing during contraction in each activation pCa solution. Equatorial small-angle X-ray diffraction patterns were collected on a CCD-based X-ray detector (Mar 165; Rayonix). The distances between the 1,0 and 1,1 equatorial X-ray reflections were converted to $d_{1,0}$ lattice spacings using Bragg's law. Lattice spacing ($d_{1,0}$) may be converted to interfilament spacing, the center-to-center distance between the thick filaments, by multiplying by $2/\sqrt{3}$. Intensities of the 1,0 and 1,1 equatorial reflections were determined from nonlinear least square fits to 1-dimensional projections of the integrated intensity along the equator. X-ray reflections were assumed to have a Gaussian peak shape with the widths constrained by those expected for a paracrystalline hexagonal lattice (3, 5).

1. Gomes AV, et al. (2006) Mapping the murine cardiac 26S proteasome complexes. *Circ Res* 99:362–371.
2. Liu H, Sadygov RG, Yates JR, III (2004) A model for random sampling and estimation of relative protein abundance in shotgun proteomics. *Anal Chem* 76:4193–4201.
3. Yuan CC, et al. (2017) Hypercontractile mutant of ventricular myosin essential light chain leads to disruption of sarcomeric structure and function and results in restrictive cardiomyopathy in mice. *Cardiovasc Res* 113:1124–1136.
4. Pacher P, Nagayama T, Mukhopadhyay P, Bátkai S, Kass DA (2008) Measurement of cardiac function using pressure-volume conductance catheter technique in mice and rats. *Nat Protoc* 3:1422–1434.
5. Yuan CC, et al. (2015) Constitutive phosphorylation of cardiac myosin regulatory light chain prevents development of hypertrophic cardiomyopathy in mice. *Proc Natl Acad Sci USA* 112:E4138–E4146.
6. Huang W, et al. (2015) Novel familial dilated cardiomyopathy mutation in MYL2 affects the structure and function of myosin regulatory light chain. *FEBS J* 282:2379–2393.
7. Mulieri LA, Hasenfuss G, Ittleman F, Blanchard EM, Alpert NR (1989) Protection of human left ventricular myocardium from cutting injury with 2,3-butanedione monoxime. *Circ Res* 65:1441–1449.
8. Wang Y, et al. (2006) Prolonged Ca^{2+} and force transients in myosin RLC transgenic mouse fibers expressing malignant and benign FHC mutations. *J Mol Biol* 361:286–299.

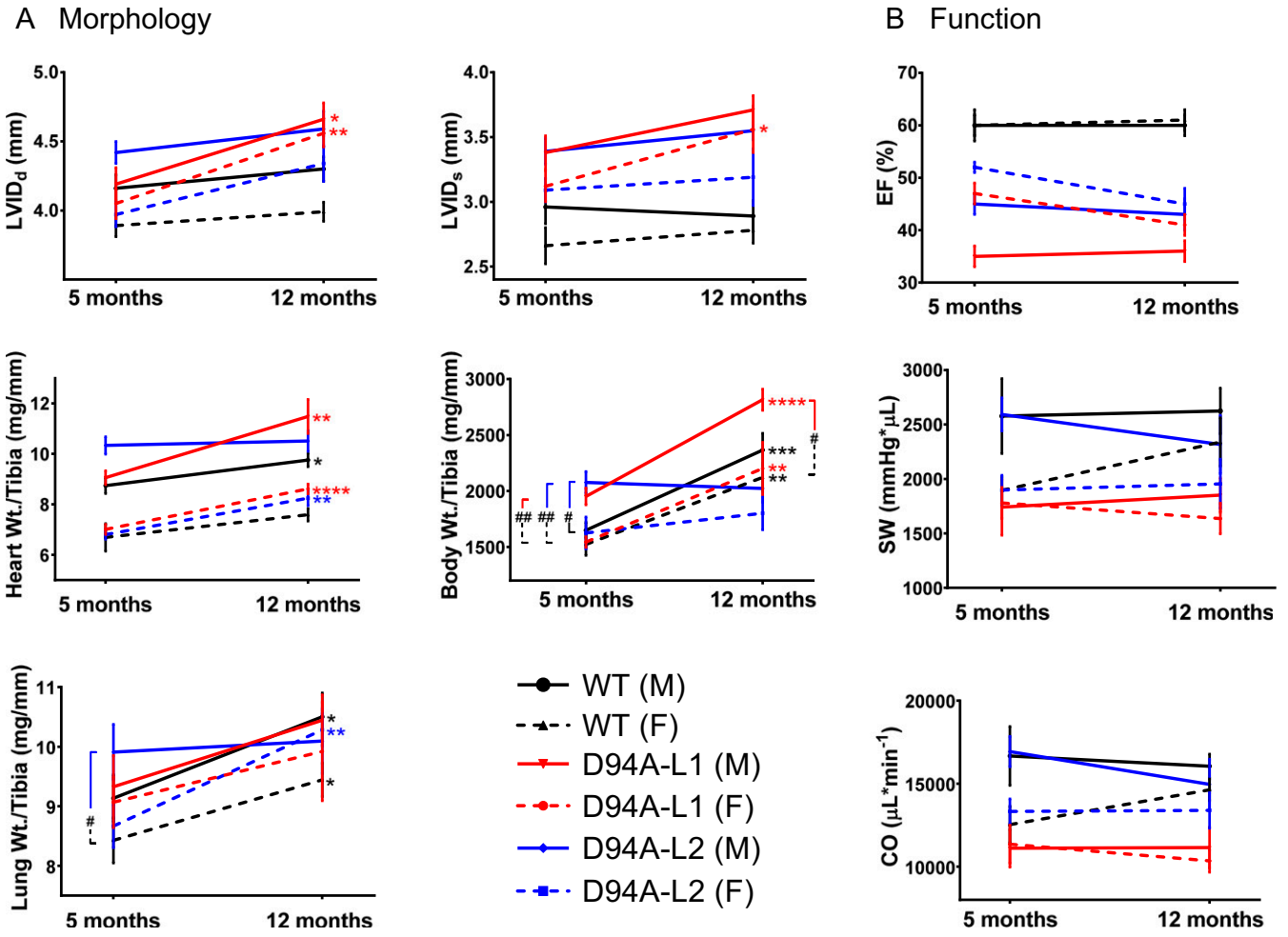

Fig. S1. Progression in morphology (*A*) and function (*B*) between 5- and 12-mo-old male and female mice assessed by plotting (*A*) LVIDd (LV inner diameter) in diastole and LVIDs in systole; heart weight/tibia length, body weight/tibia length, and lung weight/tibia length ratios; and (*B*) EF (ejection fraction), SW (stroke work), and CO (cardiac output). Except for body weight/tibia length and lung weight/tibia length ratios, the data are from Table 1 and Table S1. Statistical significance between two ages for each mouse line is depicted with $^{*}P < 0.5$, $^{**}P < 0.01$, $^{***}P < 0.001$, and $^{****}P < 0.0001$, by Student's *t* test. For body weight/tibia length and lung weight/tibia length ratios, the significance between genotypes for 5- and 12-mo-old mice is depicted with $^{\#}P < 0.5$, and $^{\#\#}P < 0.01$, by one-way ANOVA.

Table S1. Intact heart function in ∼12-mo-old D94A-RLC mice compared with WT-RLC animals by echocardiography and invasive hemodynamics

Parameter	D94A-L1-F	D94A-L2-F	WT-F	D94A-L1-M	D94A-L2-M	WT-M
Echocardiography						
No. of animals	9	8	15	8	8	14
Heart/body, mg/g	4.22 ± 0.43	4.53 ± 0.27*	3.59 ± 0.21	4.04 ± 0.17$^{\#}$	5.2 ± 0.21*	4.24 ± 0.29
Heart/tibia, mg/mm	8.61 ± 0.19*	8.24 ± 0.3*	7.59 ± 0.25	11.48 ± 0.7*,^{a}	10.51 ± 0.41^{a}	9.76 ± 0.27^{a}
HR, bpm	514 ± 10	531 ± 14	507 ± 10	492 ± 16	495 ± 28	491 ± 12
IVCT, ms	12.34 ± 1.16	15.66 ± 2.03	15.81 ± 0.97	12.15 ± 1.63	12.8 ± 2.35	15.49 ± 1.13
IVRT, ms	16.01 ± 0.91	15.19 ± 1.25	16.38 ± 1.31	18.69 ± 1.16	16.96 ± 1.27	15.64 ± 0.8
MV E/A	2.83 ± 0.35	1.55 ± 0.2	2.2 ± 0.24	1.73 ± 0.14	1.69 ± 0.22	2.06 ± 0.12
MV E/E′	−23.07 ± 2.29	−29.96 ± 2.75	−26.71 ± 2.29	−26.63 ± 2.11	−27.31 ± 1.16	−28.77 ± 1.86
EF, %	41 ± 2***	45 ± 3***	61 ± 2	36 ± 2***	43 ± 3***	60 ± 2
FS, %	22 ± 3*	27 ± 3	31 ± 2	21 ± 1***	23 ± 1**	32 ± 2
IVS;d, mm	0.76 ± 0.04	0.78 ± 0.05	0.81 ± 0.04	0.89 ± 0.05	0.85 ± 0.06	0.91 ± 0.05
IVS;s, mm	1.03 ± 0.07	1.10 ± 0.07	1.11 ± 0.04	1.18 ± 0.07	1.13 ± 0.05	1.31 ± 0.06^{a}
LVID;d, mm	4.56 ± 0.1*	4.34 ± 0.13*	3.99 ± 0.07	4.66 ± 0.12*	4.59 ± 0.13*	4.3 ± 0.09^{a}
LVID;s, mm	3.56 ± 0.18**	3.19 ± 0.22	2.78 ± 0.1	3.71 ± 0.11***	3.55 ± 0.07**	2.89 ± 0.12
LVPW;d, mm	0.74 ± 0.04	0.77 ± 0.04	0.76 ± 0.02	0.87 ± 0.03^{a}	0.88 ± 0.05	0.84 ± 0.04^{a}
LVPW;s, mm	0.97 ± 0.06	1.07 ± 0.06	1.06 ± 0.05	1.11 ± 0.07	1.19 ± 0.07	1.26 ± 0.06^{a}
Hemodynamics						
No. of animals	6	8	11	8	8	13
SW, mmHg/μL	1,636 ± 141	1,955 ± 228	2,339 ± 223	1,852 ± 160*	2,317 ± 269	2,625 ± 211
CO, μL/min	10,549 ± 741**	13,392 ± 1,075	14,630 ± 654	11,147 ± 1,236**	14,965 ± 1,514	16,055 ± 734
SV, μL	21.44 ± 1.36**,$^{\#}$	26.28 ± 2.11	29.81 ± 1.37	24.25 ± 2.27**	29.56 ± 2.39*	33.66 ± 1.87
ESV, μL	41.54 ± 4.42**	44.34 ± 3.73***	24.5 ± 2.62	50.45 ± 1.97***	47.21 ± 3.22***	29.07 ± 1.8
EDV, μL	55.04 ± 4.18	62.69 ± 2.98*	49.25 ± 3.34	68.79 ± 3.29**,^{a}	69.6 ± 2.21**	55.81 ± 2.72
Pes, mmHg	98.52 ± 2.92	91 ± 3.5	90.22 ± 5.37	100.44 ± 2.93	88.55 ± 4.51	91.49 ± 4.65
Ped, mmHg	5.06 ± 0.84	4.53 ± 0.74	4.68 ± 0.56	7.45 ± 0.8	4.51 ± 0.67	4.8 ± 1.1
HR, bpm	491 ± 6	510 ± 8	492 ± 10	457 ± 13	499 ± 21	482 ± 11
Ea, mmHg/μL	4.7 ± 0.33***,$^{\#}$	3.57 ± 0.18	3.04 ± 0.16	4.36 ± 0.36***,$^{\#}$	3.09 ± 0.19	2.78 ± 0.15
Ea/Ees	1.51 ± 0.4	1.12 ± 0.13	1.2 ± 0.18	1.54 ± 0.1	0.87 ± 0.13	1.18 ± 0.17
dP/dt_{max}, mmHg/s	9,237 ± 686	8,527 ± 557	8,976 ± 647	8,286 ± 655	8,686 ± 577	8,772 ± 433
dP/dt_{min}, mmHg/s	−9,159 ± 823	−9,175 ± 626	−8,061 ± 572	−8,164 ± 652	−8,439 ± 689	−8,180 ± 494
Tau, ms	6.11 ± 0.36	5.78 ± 0.16	6.07 ± 0.21	7.06 ± 0.73	5.77 ± 0.25	6.02 ± 0.29
No. of animals	6	8	10	6	8	11
ESPVR	3.54 ± 0.67	3.49 ± 0.4	3.1 ± 0.42	2.81 ± 0.24	4.03 ± 0.56	2.86 ± 0.32
EDPVR	0.19 ± 0.04	0.1 ± 0.01	0.1 ± 0.02	0.15 ± 0.03	0.12 ± 0.02	0.15 ± 0.02
PRSW	51.27 ± 6.44	64.17 ± 4.71	64.14 ± 6.63	63.39 ± 4.51	75.83 ± 5.85	66.15 ± 5.2
dP/dt_{max}–EDV	211 ± 47	134.34 ± 14.72	147.54 ± 28.04	151.59 ± 24.31	154.94 ± 15.72	130.79 ± 13.39

Heart weight/body weight (in mg/g); heart weight/tibia length (in mg/mm); CO, cardiac output; d, diastolic; dP/dt_{max}, peak rate for pressure rise; $-dP/dt_{min}$, peak rate for pressure decline; Ea, arterial elastance; EDPVR, slope of end-diastolic PV relationship; EDV, end-diastolic volume; Ees, end-systolic elastance, slope of ESPVR (end-systolic pressure–volume relationship); EF, ejection fraction; ESV, end-systolic volume; FS, fractional shortening; HR, heart rate (in beats per min); IVCT, isovolumetric contraction time; IVRT, isovolumetric relaxation time; IVS, interventricular septum; LVID, left ventricular (LV) inner diameter; LVPW, LV posterior wall; Ped, end-diastolic pressure; Pes, end-systolic pressure; PRSW, slope of SW–EDV relationship; s, systolic; SV, stroke volume; SW, stroke work; Tau, relaxation time constant. Data are the mean ± SEM. *$P < 0.05$, **$P < 0.01$, and ***$P < 0.001$ D94A vs. WT and $^{\#}P < 0.05$ L1 vs. L2, by one-way ANOVA and the post hoc Tukey's multiple comparison test; $^{a}P < 0.05$ M vs. F, by Student's *t* test.

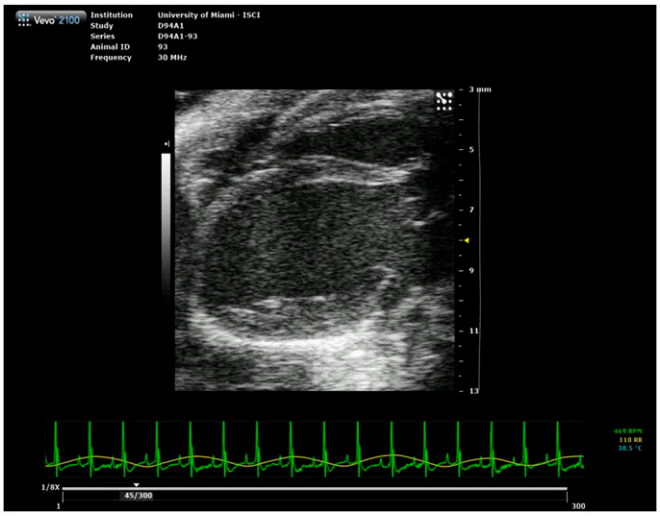

Movie S1. Representative 2D echocardiography images (B mode) of parasternal long-axis view of the LV of a 5-mo-old D94A-L1-M mouse. Body weight, 31.49 g; average recorded heart rate (HR), 475 bpm; ejection fraction (EF), 35%; as calculated by the measure of LV volume in diastole and systole.

Movie S1

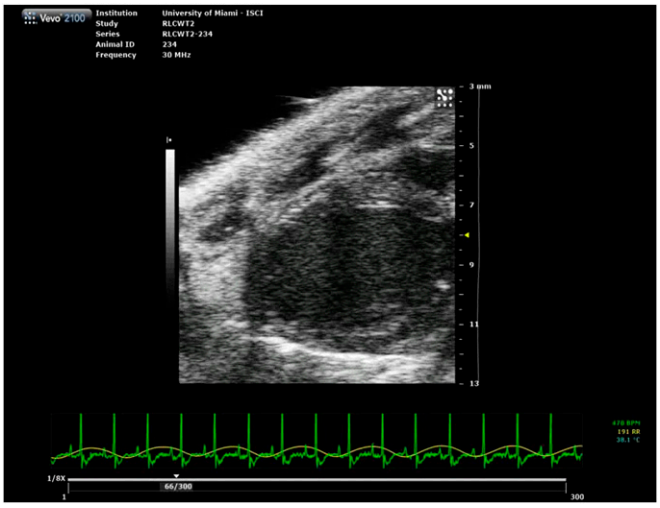

Movie S2. Representative 2D echocardiography images (B mode) of parasternal long-axis view of the LV of a 5-mo-old WT-M mouse. Body weight, 30.93 g; average recorded HR, 467 bpm; EF, 61%; as calculated by the measure of LV volume in diastole and systole.

Movie S2